



HAL
open science

Thermodynamic analyses on hybrid sorption cycles for low-grade heat storage and cogeneration of power and refrigeration

Alexis Godefroy, Maxime Perier-Muzet, Nathalie Mazet

► **To cite this version:**

Alexis Godefroy, Maxime Perier-Muzet, Nathalie Mazet. Thermodynamic analyses on hybrid sorption cycles for low-grade heat storage and cogeneration of power and refrigeration. *Applied Energy*, 2019, 255, pp.113751. 10.1016/j.apenergy.2019.113751 . hal-02332649

HAL Id: hal-02332649

<https://hal.science/hal-02332649>

Submitted on 24 Oct 2019

HAL is a multi-disciplinary open access archive for the deposit and dissemination of scientific research documents, whether they are published or not. The documents may come from teaching and research institutions in France or abroad, or from public or private research centers.

L'archive ouverte pluridisciplinaire **HAL**, est destinée au dépôt et à la diffusion de documents scientifiques de niveau recherche, publiés ou non, émanant des établissements d'enseignement et de recherche français ou étrangers, des laboratoires publics ou privés.

Thermodynamic analyses on hybrid sorption cycles for low-grade heat storage and cogeneration of power and refrigeration

Alexis Godefroy^{a,b}, Maxime Perier-Muzet^{a,b}, Nathalie Mazet^{a*}

^aCNRS-PROMES Laboratoire PROcédés, Matériaux et Energie Solaire, Tecnosud, Rambla de la Thermodynamique, 66100 Perpignan, France

^bUPVD Université de Perpignan Via Domitia, 52 Avenue Paul Alduy, 66100 Perpignan, France

*Corresponding author

E-mail addresses: alexis.godefroy@univ-perp.fr (A. Godefroy), maxime.perier-muzet@univ-perp.fr (M. Perier-Muzet), mazet@univ-perp.fr (N. Mazet).

Abstract

This paper investigates three ways of coupling a solid/gas sorption refrigeration cycle with a Rankine cycle to create innovative hybrid cycles enabling power and refrigeration cogeneration with intrinsic energy storage. A new methodology has been developed to analyze these hybrid cycles and assess five relevant performance criteria (required heat source temperature, energy efficiency, exergy efficiency, power production ratio, and exergy storage density). Screening of 103 reactive salts implemented in the different hybrid cycle configurations highlights the most favorable configuration and reagent to meet the requirements of various applications. Analyses show that energy and exergy efficiencies can reach 0.61 and 0.40, respectively. Exergy storage density ranges from 142 to 640 kJ/kg_{NH₃} when the heat source temperature is increased from 107 °C to 250 °C.

Keywords: thermochemical cycles, sorption, hybrid cycles, power and refrigeration cogeneration, thermal storage, thermodynamic analysis

Nomenclature

Symbols

c	Mass heat capacity of a solid ($J \cdot kg^{-1} \cdot K^{-1}$)
$\Delta_r H$	Reaction enthalpy ($J \cdot mol^{-1}$)
$\Delta_r S$	Reaction entropy ($J \cdot mol^{-1}$)
ΔS_{vap}	Vaporization entropy ($J \cdot mol^{-1} \cdot K^{-1}$)
ΔT	Temperature pinch (K)
ΔX	Variation range of reaction rate (–)
Ex	Exergy quantity (J)
ex	Specific exergy quantity ($J \cdot kg^{-1}$)
h	Specific enthalpy ($J \cdot kg^{-1}$)
L_{vap}	Vaporization enthalpy ($J \cdot mol^{-1}$)
M	Molar mass ($kg \cdot mol^{-1}$)
m	Mass (kg)
n	Amount of matter (mol)
P	Pressure (Pa)
Q	Heat (J)
q	Specific heat ($J \cdot kg^{-1}$)
R	Ideal gas constant ($J \cdot mol^{-1} \cdot K^{-1}$)
R_v	Volumetric expansion ratio (–)
s	Specific entropy ($J \cdot kg^{-1} \cdot K^{-1}$)
T	Temperature (K)
V	Volume (m^3)
W	Mechanical work (J)
w	Specific work ($J \cdot kg^{-1}$)
x	Vapor quality (–)

Greek letters

ε	Composite porosity (–)
η	Efficiency (–)
ν	Stoichiometric coefficient (–)
ρ	Density ($kg \cdot m^{-3}$)
τ	Ratio (–)

Superscripts

0	Reference conditions
---	----------------------

Subscripts

I	Energy-related
amb	Ambient level
$cold$	Cold
$comp$	Composite reactive material
$cond$	Condensation
r	Chemical reaction
$cycled$	Involved in one complete cycle
dec	Decomposition
eq	Thermodynamic equilibrium
$evap$	Evaporation
ex	Exergy-related
H/HTM	High Temperature Material
hot	Hot source level
$HX1$	Liquid/liquid or liquid/vapor heat exchange
$HX2$	Vapor/vapor heat exchange

<i>in</i>	Input (energy or exergy)	<i>synth</i>	Synthesis
<i>is</i>	Isentropic	<i>w</i>	Work production
<i>L/LTM</i>	Low Temperature Material		
<i>LV</i>	Liquid/vapor phase change		
<i>max</i>	Maximal value		
<i>met</i>	Metal of the chemical reactor		
<i>min</i>	Minimal value		
<i>nom</i>	Nominal value		
<i>p</i>	Poor (reactive salt after decomposition)		
<i>perfect</i>	'Perfect' case		
<i>r</i>	Rich (reactive salt after synthesis)		
<i>salt</i>	Reactive salt (HTM or LTM)		

1. Introduction

Renewable energy sources are an attractive solution to the problem of scarce fossil resources and the challenge of cutting greenhouse gas emissions, but industrial waste heat (typically from steel and glass industry or power plants) is another huge but under-exploited energy pool [1]. The low-grade heat resource available and several ways of recovering this energy were thoroughly investigated by Ling-Chin et al. [2]. However, the availability of these energy sources is very often variable.

Needs also fluctuate strongly on the energy demand side, not only over time but also in energy form: demands such as electricity, cooling and heating need to be covered at different time-scales with different energy levels. Efficiently matching these *sources* and *needs* requires suitable energy storage systems. Stutz et al. [3] reviewed existing thermal solar energy storage systems, and Nadeem et al. [4] recently completed a detailed comparative review of existing energy storage systems.

The net result is that we have a major energy management issue to address in order to make the best use of these renewable energy sources and industrial waste heat to meet wider form and quantity of energy demands. This paper focuses on these under-exploited low-grade heat sources, chiefly solar thermal sources (concentrated or not) and industrial waste heat, targeting temperatures up to $T_{hot,max} = 250^{\circ}C$. The aim is to store the thermal energy of these sources and convert it into one or more useful effects, chiefly electric power and cooling according to demand. The technical solutions presented here could be used in embedded applications, especially for the delivery of refrigerated goods in urban areas using electric vehicles.

The conversion of low-grade heat into cold has been widely investigated, leading to tri-thermal cycles involving sorption processes as a relevant way forward, as evidenced in [5] and [6]. Two types of sorption cycles can meet cold production requirements:

- Liquid/gas absorption cycles (typically using LiBr/H₂O or H₂O/NH₃ solutions)
- Solid/gas adsorption cycles (typically using NH₃/activated carbon or H₂O/silica gel) or thermochemical cycles (using ammonia salt/NH₃ working pairs for example)

Note that the storage function can only be intrinsically achieved by the second type of sorption cycles (solid/gas sorption cycles). Indeed, the absorption process works continuously (the liquid solution circulates between a gas absorber and a desorber) whereas the solid/gas sorption process intrinsically works discontinuously as the reactive solid is usually implemented in a fixed-bed reactor. These solid sorption cycles involve two operation steps that are shifted in time, thus enabling storage of the input low-grade heat in the first working step (by endothermal desorption: charging step) and cooling production in the second step (discharging step). Moreover, due to the wide diversity of available reactants, solid/gas thermochemical cycles can use lower-temperature heat sources than other sorption cycles. Among them, systems based on ammonia salt/NH₃ pairs afford the added advantage of using a refrigerant with a zero Global Warming Potential (GWP) and zero Ozone Depletion Potential (ODP).

Low-grade heat can also be converted into mechanical work (for power production purposes) using an Organic Rankine Cycle (ORC) or a similar power cycle.

Therefore, one possible way to implement a process combining low-grade heat storage and conversion into several forms is to create a **hybrid** thermodynamic cycle. Basically, the **hybridization** of several independent thermodynamic cycles consists in sharing their common physical components (such as evaporator, condenser, chemical reactor, and working fluid) in a single cycle, thus combining the advantages and features of each cycle at potentially less cost than when using two separate systems. Hybrid thermodynamic cycles are attracting increasing attention from research aiming to develop novel multi-purpose systems, but the concept is still only emerging and the Technological Readiness Level (TRL) is relatively low (at 2–3). Here we bring innovation to the current body of knowledge on hybrid cycles by developing a broader approach of hybrid cycles based on solid/gas thermochemical and power cycles.

Section 2.2 reviews the state of the art in the field of hybrid sorption cycles providing power and refrigeration cogeneration. Early investigations focused on the hybridization of a liquid/gas absorption refrigeration cycle with a power cycle. As detailed in §2.2., several systems have been theoretically and experimentally studied, some of them using a low-grade heat source (see especially [7] and [8]). However, as mentioned above, liquid/gas absorption cycles operate continuously and so cannot provide a storage feature. Their maximal thermal and exergy efficiencies are around 0.25 and 0.65, respectively. Later investigations proposed other hybrid systems based on solid/gas sorption cycles (adsorption or thermochemical cycles) that bring together power and cold cogeneration with an intrinsic storage feature. The state of the art in these systems (see §2.2. for details) reveals a very broad range of energy and exergy performances, as the existing

literature considers very different assumptions and operating conditions. Thus, maximal efficiency values are not provided for hybrid thermochemical cycles, since any comparison with other sorption systems would be unfair. The very few studies carried out on hybrid thermochemical cycles are based on a thermodynamic analysis focusing only on two main performance criteria (energy and exergy efficiencies) and a few reactive salts (see especially the theoretical studies [9, 10] and the experimental setup investigated in [11]). Nevertheless, these cycles prove suitable for low-grade heat use and demonstrate relatively good energy and exergy performances.

This paper expands the concept of hybrid thermochemical cycle by defining three ways of hybridizing a solid/gas thermochemical refrigeration cycle with a vapor power cycle in order to engineer innovative cycles combining a refrigeration and power cogeneration cycle with an intrinsic energy storage function. A wider thermodynamic analysis of these three hybrid cycles (referred to as **modes**) is developed, based on an original approach: a set of five relevant performance criteria is investigated to account for the various features of the cycles (power production, cold production, and storage). Moreover, a large set of solid reactants (103 reactive salts) is screened. This study leads to an exhaustive comparative assessment of the performances for the whole set of criteria, modes and reactants. This thermodynamic analysis serves to identify the most relevant modes and reactive salts for various fields of application (according to low-grade heat source temperature and specific needs). The paper thus addresses a significant gap with respect to the current body of knowledge in terms of configurations, reactants and performance criteria for hybrid thermochemical cycles for power and refrigeration cogeneration.

The paper starts by overviewing the working principle and state of the art in hybrid sorption cycles for power and cold production. Then, we depict the three **modes** of hybridizing solid/gas thermochemical and power cycles in order to build a cogeneration cycle. Next, the thermodynamic analysis model and methodology are presented and the relevant parameters and performance criteria are defined. The paper goes on to report the results and analyses of this thermodynamic study, leading to different energy purposes: for the three **modes** (**separated** power and cold production mode, **simultaneous** power and cold production mode, **combined** mode), the operating conditions and performances are summarized and analyzed. These results are then discussed through a sensitivity study of some key variables, and we interpret and compare the operating conditions and performances of all the hybrid cycles investigated. In the conclusion, the most relevant applications for each hybrid cycle are proposed, and the prospects for these investigations are sketched out.

2. State of the art and configurations of hybrid cycles involving a sorption process

2.1. General working principle

The principle can be described by starting from a sorption refrigeration cycle, which is illustrated in *Fig. 1* and *Fig. 2* for hybridization of a liquid/gas absorption cycle and a solid/gas thermochemical cycle, respectively, with a power cycle. As a rule, these hybridizations lead to configurations whose main components are:

- 2 vapor generators, where endothermal processes occur: one operating at high pressure (with a heat supply Q_{in} from a heat source at T_{hot}), and the other operating at low pressure (removing Q_{cold} from the medium to be cooled at T_{cold}).
- 2 vapor absorbers, where exothermal processes occur: one at high pressure and the other at low pressure. Both release heat at T_{amb} or at an intermediate temperature T_m .
- 1 or several expanders for power production.

This general principle leads to two different cycles, depending on the type of sorption process:

- A hybrid cycle based on a liquid/gas absorption cycle (*Fig. 1*) works continuously, as the liquid solution containing the sorbent circulates between vapor absorber and vapor generator. The expander can be located either (i) on the vapor flow between the high-pressure vapor generator and the high-pressure vapor absorber, resulting in power production then cold production in series; or (ii) between the high-pressure vapor generator and the low-pressure vapor absorber. In this configuration, the working fluid flow is split between the expander and the vapor absorber and generator on the left side of *Fig. 1*, leading to parallel power and cold production.
- A solid/gas sorption hybrid cycle (*Fig. 2*) is intrinsically discontinuous, as it uses a solid sorbent. It involves two time-shifted operating steps, which provides its intrinsic storage function: a charging step when a heat source is available, then a discharging step. The expander can operate in one or both steps. Furthermore, the low-temperature endothermal process (in the discharging step) may lead to cold production. This kind of hybrid cycle can therefore operate according to three modes: (i) **separated** power and cold production mode, when the expander operates in the charging step while cold is

produced in the discharging step; (ii) **simultaneous** cold and power production mode, when the expander operates only in discharging step alongside cold production; (iii) **combined** mode, when the two previous modes are combined, leading to power productions in both steps and cold production in the discharging step.

Note that the vapor absorber and desorber can be chosen in different ways:

- For the absorption hybrid cycle: the right-side components on Fig. 1 are a liquid/gas desorber and absorber, while the left-side components are a condenser and an evaporator;
- For the solid/gas sorption hybrid cycle (Fig. 2): the right-side component, operating at high temperatures, must be a solid/gas reactor, while the left-side component can be either another solid/gas reactor operating at lower temperature (this process is named *resorption* cycle) or a reactive fluid condenser/evaporator (named *single sorption* cycle).

For a general description of the various hybrid cycles (in the following sections of this paper), the material in the component requiring the high temperature source will be called **High Temperature Material (HTM)**, right-side material on Fig. 2, Fig. 3, Fig. 5 and Fig. 7) while the material in the other component operating with the low temperature source will be called **Low Temperature Material (LTM)**, in the left-side component).

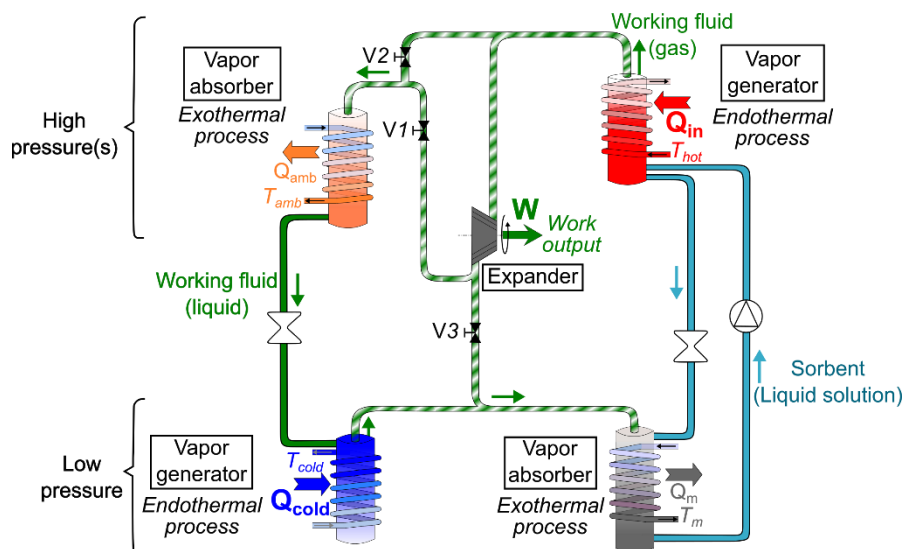


Fig. 1 – Liquid/gas absorption hybrid cycle for power and cold cogeneration: operating principle. Power and cold production in series (valve V1 open, V2 and V3 closed) or in parallel (V1 closed, V2 and V3 open)

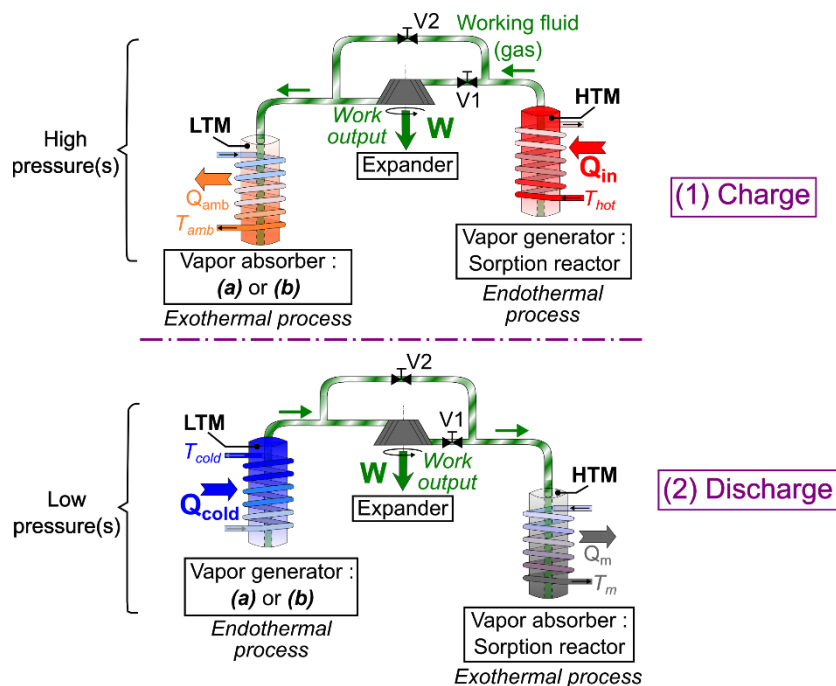


Fig. 2 – Solid/gas sorption hybrid cycle for power and cold cogeneration: operating principle.

- **Separated** power and cold production mode: in the charging step, valve V1 open and valve V2 closed.
In the discharging step, valve V1 closed and valve V2 open (Fig. 3 and Fig. 4)
 - **Simultaneous** power and cold production mode: in the charging step, valve V1 closed and valve V2 open.
In the discharging step, valve V1 open and valve V2 closed (Fig. 5 and Fig. 6)
 - **Combined** mode: in both steps, valve V1 open and valve V2 closed (Fig. 7 and Fig. 8)
- (a) Resorption cycle (2 sorption reactors) – (b) Single sorption cycle (only 1 sorption reactor and 1 evaporator/condenser)

2.2. State of the art

The **first hybridization of a sorption cycle** with a power cycle was implemented by Goswami et al. [7]. Their combined cooling and power cycle is based on a liquid/gas ($\text{H}_2\text{O}/\text{NH}_3$) absorption cycle coupled with an expander for power generation. It is suitable for use with a low-grade solar heat source (heat source temperature used for calculations is 140°C). The main output is mechanical work (about 74% of the total output energy), and an additional cooling effect occurs at the expander outlet by exploiting the low temperature flow of the working fluid (cold production temperature is set at -10°C). The energy efficiency is $\eta_l = 0.24$, and the exergy efficiency (computed with data available from [7]) is $\eta_{ex} = 0.59$. Moreover, a cogeneration performance optimization study on this cycle is performed in [12], using a second-law-based criterion as the objective function. Moreover, an experimental setup [8] was built and a good agreement was found with theoretical predictions: energy and exergy efficiencies computed from experimental data were respectively 0.25 and 0.65. Later, several hybrid absorption cycles developed for power and cold cogeneration were compiled by Ayoub et al. [13] for systems with $\text{H}_2\text{O}/\text{NH}_3$ as working pair. This paper highlights the broad diversity of performances with available cycles (various heat-source temperatures and power-to-cooling ratios).

More recently, Ventas et al. [14] investigated the performances of a double-effect hybrid cycle based on liquid/gas ($\text{NH}_3/\text{LiNO}_3$) absorption coupled with an expander for power production. Their system makes it possible to adjust vapor flow through the expander, and thus the power-to-cooling ratio. Working under 150°C heat source temperature and providing cold at -5°C , it achieves energy and exergy efficiencies of 0.61 and 0.56, respectively. At these performance levels, the main output is cold (about 90% of the total useful energy).

On the other hand, Ziegler et al. [15] borrowed the Honigmann system to develop a broader hybrid cycles approach involving any kind of sorption process (absorption, adsorption or chemical reaction). They proposed a generalized cycle configuration including four main components (condenser, evaporator, desorber, ab- or adsorber) and an expander, allowing flexible inputs (heat or work) and outputs (work or cold) as well as a possible storage function. Then, using liquid/gas absorption (with $\text{LiBr}/\text{H}_2\text{O}$ and $\text{NaOH}/\text{H}_2\text{O}$ as working pairs), they performed dynamic simulations of a power cycle with a storage function (storage of the working fluid) [16].

Concerning **hybrid cycles involving solid/gas chemical reaction**, the system that has been addressed most so far is the resorption cycle (case (a) on Fig. 2). This cycle associates two reactive beds involving two different solid salts reacting with the same gas, i.e. a Low Temperature Material (LTM) and a High Temperature Material (HTM), whose reaction equilibrium temperature is higher than that of the LTM at a given pressure. See §2.3. for an in-depth description of hybrid solid/gas thermochemical cycles. This state of the art review focuses on the use of ammonia as reactive vapor.

Several studies have investigated resorption cycles for power production only. Bao et al. [17] designed a cycle using ultra-low-grade heat (source temperature from 30°C to 100°C) to generate power, using a compressor to drive the decomposition. Overall energy efficiency ranged from 0.47 to 0.62 and exergy efficiency ranged from 0.60 to 0.90, depending on heat source temperature. Later, the same authors compared a pumpless ORC with resorption power cycles [18], and evaluated the output work per mass unit of working fluid as 100 to 550 kJ/kg for the resorption cycle against 10 to 100 kJ/kg for a pumpless ORC. They highlighted that the difference between these specific values was linked to the small molecular weight of ammonia compared with the organic fluid used in ORC. Using a low-grade heat source between 60°C and 180°C , the energy efficiencies ranged from 0.08 to 0.25 for pumpless ORC but were much lower (0.06–0.17) for the resorption cycle, due to the wet property of ammonia which prevents exploiting the whole available pressure ratio (considering only one expansion stage). This can be overcome by the multiple-expansion resorption power generation that Bao et al. also investigated in [19]. Using a heat source between 30°C and 150°C and 2 to 4 expansion stages, they achieved a slightly higher work output per unit mass of working fluid (from 100 to 600 kJ/kg) but similar energy efficiencies (0.06–0.15) as previously. One of the main findings of this work was the need to find a trade-off between more total work output (more expansions) and a more compact system with higher average output per expansion device.

Lu et al. [20] designed a system involving two resorption cycles operating in phase opposition, recovering low-grade heat from two heat sources, at 180–200 °C and 80–90 °C, and enabling continuous operation. The reactive ammonia salts MnCl_2 and SrCl_2 were chosen as working pair and led to a thermal efficiency of about 0.11 in each mode. Their detailed dynamic study [21] stressed the importance of the coupling between expander and chemical reactor and the need to manage coupling pressure in order to control the power output. Jiang et al. [22] proposed an improvement of resorption cycles using a new composite sorbent that enhances the reactor kinetics, and they obtained energy efficiencies ranging from 0.11 to 0.14 and exergy efficiencies from 0.62 to 0.81, with a heat source temperature between 80 °C and 110 °C.

Closer to our focus here, a few resorption cycles have been investigated for power and cold cogeneration. Wang et al. [9] evaluated the energy and exergy performances of this kind of resorption cycle for 9 different reactive pairs and for a heat source temperature between 100 °C and 400 °C, with cold production temperature set at 10 °C. The best performances were obtained with $\text{SrCl}-\text{BaCl}_2$ as working pair, the Coefficient Of Performance (COP: performance indicator for cold production) ranged from 0.55 to 0.78, and exergy efficiency (considering both power and cold production) ranged from 0.81 to 0.90. Jiang et al. [11] proposed both theoretical and experimental investigations for a system using $\text{MnCl}_2-\text{CaCl}_2$ as reactive salts, and a heat source temperature between 120 °C and 180 °C. Moreover, they added a Phase Change Material tank to provide an energy storage function [23], and employed a scroll expander as it suits smaller power generation levels. Nevertheless, the highly dynamic behavior of the chemical reactions makes it hard to control the power output of this system. The experimental COP ranged from 0.27 to 0.37 and total exergy efficiency from 0.12 to 0.16. Lu et al. [24] performed a thermodynamic analysis of a resorption cycle using mass and heat recovery processes in order to improve cycle performances. After setting refrigeration temperature at 10 °C and heat source temperature at 100–300 °C, one of the best working pairs was $\text{MnCl}_2-\text{BaCl}_2$ (COP 0.74–0.82). Finally, Jiang et al. [10] recently demonstrated the huge potential of hybrid thermochemical cycles for low-grade heat utilization: they proposed a novel resorption cycle, integrating internal heat recovery to improve energy performances in comparison with existing resorption systems. Using heat source temperatures in the range 200–360 °C and providing a refrigeration effect at 0 °C, this cycle gives a COP of 1.3 and exergy efficiencies between 0.41 and 0.74.

The second hybrid thermochemical cycle configuration, named single sorption cycle (case **b.** on Fig. 2), has been less investigated. Unlike the resorption cycle, a single sorption cycle involves only one solid/gas chemical reaction coupled with the liquid/vapor phase change of the same gas (ammonia). Consequently, the low-pressure vapor generator is an evaporator and the high-pressure vapor absorber is a condenser. This kind of configuration favors low-temperature cold production. One of the main analyses was completed by Bao et al., who first proposed a theoretical study [25] then an experimental investigation using a scroll expander [26]. Their cycle (see Fig. 2) runs in **separated** mode, and the heat source temperature range is 150–200 °C. The results again highlight the difficulty involved in coupling expander to chemical reactor: instead of obtaining the expected power output at 1000 W with a 0.01 kg/s mass flow rate of ammonia, power generation proved unstable and power output only reached a maximal value of 490 W.

Among hybrid thermochemical cycles, very few configurations have been investigated and they are mainly related to resorption cycles. The present work therefore investigates novel configurations that can provide significant improvements over the existing systems, such as easier technical implementation (especially in single sorption cycles) or the ability to store and/or increase power production. In terms of applications, the studied systems show a huge potential for cold production (cooling represents more than 70 % of produced useful effects).

2.3. Details on hybridizing a solid/gas sorption cycle with a power cycle

The thermodynamic analyses are performed for both resorption cycles (2 sorption reactors – see Fig. 2, case **a.**) and single sorption cycles (1 sorption reactor only – see Fig. 2, case **b.**). Ammonia is chosen as the working fluid (it is the reactive gas of the chemical reactions). The general layout of solid/gas sorption hybrid cycles, as presented on Fig. 2, defines the location of the heat input (Q_{in}) and cold production (Q_{cold}) in the cycle. In addition, expansion devices operation can define three working modes for the hybrid cycle, that are detailed in different sections of this paper:

- **Separated** power and cold mode: work output occurs in the charging step (the discharging step is isobaric) (see §4.).
- **Simultaneous** power and cold mode: work output occurs in the discharging step (the charging step is isobaric) (see §5.).
- **Combined** mode: work output occurs in both the charging and discharging steps (see §6.).

The following sections 4 to 6 present the thermodynamic analyses of these three modes (developed in a similar manner) and discuss their advantages and difficulties in practice. Both resorption and single sorption cycles are considered for each mode. These various modes and configurations are then compared in §7.

2.3.a. Separated power and cold production mode: description of the cycle and thermodynamic path

For the **separated** power and cold production mode, the pattern of the cycle (thermodynamic path of the working fluid) is plotted on a Clausius-Clapeyron diagram on Fig. 3. This diagram highlights the two distinct operating steps and their corresponding temperature and pressure levels, as well as input and output energies. The thermodynamic path is also plotted on the schematic T-s diagram of ammonia (Fig. 4) to give a more complete picture of the cycle, as Fig. 3 does not account for entropy variations of the working fluid. As described in §2.1, the hybrid sorption cycle uses two active materials: the LTM and the HTM. They are involved either in a solid/gas chemical reaction or in a liquid/gas phase change according to cycle configuration (either a *resorption* or a *single sorption* cycle). The corresponding thermodynamic equilibrium curves of these reactions or phase changes are plotted on both diagrams.

During the charging step (points 13 to 6), a heat source is needed to heat the reactor containing HTM to T_{hot} (heat supply Q_m). Opening valve V1 (see Fig. 2) between the vapor generator, expander and absorber brings HTM out of its thermodynamic equilibrium state (point 1), therefore triggering the endothermal decomposition reaction and generating a superheated ammonia vapor at high pressure $P_{dec,H}$ (point 2). The vapor flow leaving the reactor is then expanded to a lower pressure (point 3), producing the mechanical work W . Expanded ammonia at pressure P_4 finally flows towards the vapor absorber containing LTM, where the non-equilibrium temperature and pressure conditions allow the exothermal synthesis reaction (or condensation) to occur (points 4-5-6). Heat Q_{amb} is rejected at ambient temperature level T_{amb} .

During the discharging step (points 7 to 12), the respective roles of vapor generator and absorber are reversed. Opening valve V2 between these two components imposes a pressure level P_7 in both components, which brings LTM and HTM out of their thermodynamic equilibrium states: a refrigeration effect Q_{cold} is provided by the endothermal decomposition reaction (or evaporation) of LTM (points 7-8-9), then the generated ammonia vapor flows towards the vapor absorber containing HTM, where the non-equilibrium temperature and pressure conditions enable the exothermal synthesis reaction to occur (points 10-11-12). Heat Q_m is rejected at an intermediate temperature level T_m .

The transient step (switching from charging to discharging step) is achieved as follows: (i) vapor generator and absorber are disconnected, (ii) they are brought respectively to intermediate heat sink temperature T_m and cold source temperature T_{cold} and the temperature decreases result in pressure decreases, since LTM and HTM thermodynamic equilibria are monovariant, (iii) the components are connected again and the pressure equalization (at $P_9 = P_{10}$) brings them out of their thermodynamic equilibria, which enables carrying out the discharging step. The reverse transient step (switching from discharging to charging step) is achieved in a similar way.

Note that the T-s diagram (Fig. 4) serves to discriminate between several pairs of points with the same pressure and temperature but different specific entropies of the working fluid (points 4-5, 7-8, 11-12 and 13-1). On this diagram, the LTM and HTM equilibrium curves give the temperature and entropy of ammonia in absorbed (or saturated liquid) state (left) and desorbed (or saturated vapor) state (right). They are obtained using thermochemical data for the salt and suitable assumptions. Neveu et al. [27] detailed a method to build these thermodynamic equilibrium curves of sorption reactions for ammonia salts in several thermodynamic diagrams.

Moreover, Fig. 3 and Fig. 4 feature several temperature pinches:

- Temperature pinches ΔT_{HX1} and ΔT_{HX2} for heat exchange with the heat sources or sinks.
- Temperature deviations from thermodynamic equilibrium curves, ΔT_{r-eq} and ΔT_{LV-eq} .

These temperature pinches have to be considered in real processes. More details on these parameters are given in §3.2.a.

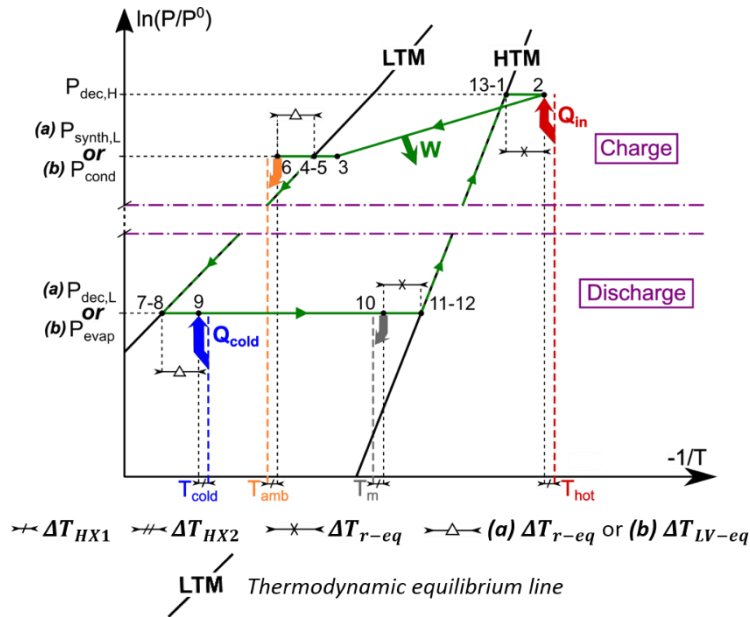


Fig. 3 – Separated power and cold production mode of a hybrid solid/gas chemical reaction cycle: thermodynamic path in a Clausius-Clapeyron diagram.

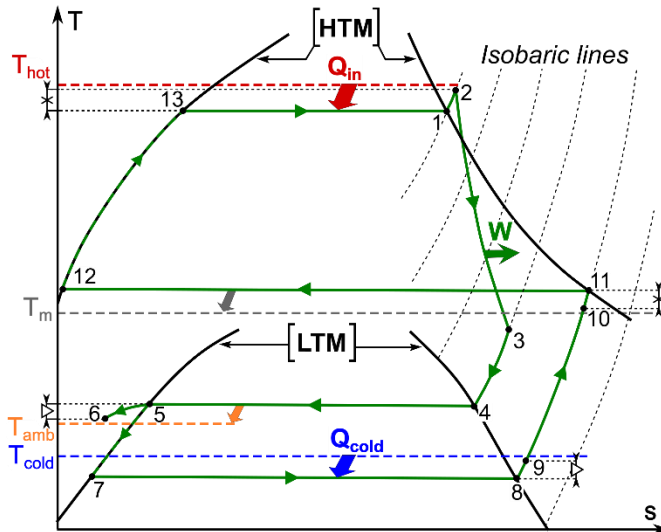


Fig. 4 – Separated power and cold production mode of a hybrid solid/gas chemical reaction cycle: thermodynamic path in the T-s diagram of ammonia (see Fig. 3 for captions).

2.3.b. Simultaneous power and cold production mode: cycle and thermodynamic path

For the **simultaneous** power and cold production mode, as in §2.2.a., the pattern of the cycle is given on a Clausius-Clapeyron diagram in Fig. 5 and the thermodynamic path of the working fluid is also plotted on a T-s diagram on Fig. 6.

In contrast to the separated mode, the charging step (points 9 to 14) is isobaric and does not provide any power production. Heat Q_{in} is supplied at the HTM reactor to achieve its endothermal decomposition reaction (points 9-10) and generate a superheated ammonia vapor (point 11); this vapor at pressure P_{11} directly flows towards the LTM vapor absorber where the exothermal synthesis reaction (or condensation) takes place (points 12-13-14). Like in the separated mode, heat Q_{amb} is thus rejected at the ambient temperature T_{amb} .

During the discharging step (points 15 to 8), both useful effects (refrigeration effect and power generation) are produced. When the valve V1 between LTM vapor generator and HTM vapor absorber is opened, the in-component pressures change, which brings LTM and HTM out of their equilibrium states. This triggers the endothermal decomposition reaction (or evaporation) of LTM (points 15-1-2), providing a refrigeration effect Q_{cold} and releasing ammonia vapor. However, instead of flowing towards the HTM vapor absorber, this vapor at pressure P_2 is superheated before entering the expander (point 3) and providing mechanical work W (points 3-

4). The expanded ammonia at $P_{synth,H}$ (point 4) often reaches very low temperatures, which may serve for additional cold production (points 4-5). Finally, the exothermal synthesis reaction of HTM occurs (point 6) and absorbs this ammonia flow. Note that heat Q_m released by this exothermal reaction is partially used to superheat the ammonia vapor upstream the expander (from T_{amb} to point 3) in order to reduce the liquid fraction at the expander outlet (point 4), with the surplus heat getting rejected at intermediate temperature T_m .

Compared with the separated mode, we would expect a lower cycle high pressure value ($P_{11} = P_{12}$), because there is no expansion stage in the charging step. Since the expansion device is located in the discharging step, the low pressure of the cycle ($P_4 = P_7 = P_{synth,H}$) should reach low values. This low pressure may cause mass transfer limitations inside the porous reactive bed in this step, which the HTM reactor design has to prevent.

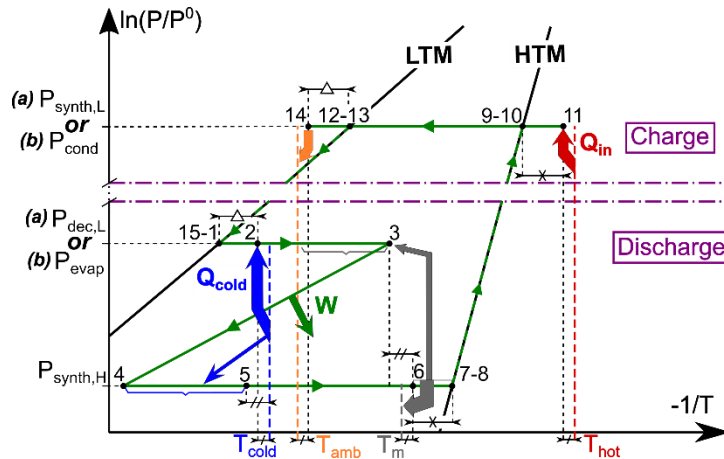


Fig. 5 – Simultaneous power and cold production mode of a hybrid solid/gas chemical reaction cycle: thermodynamic path in a Clausius-Clapeyron diagram (see Fig. 3 for captions).

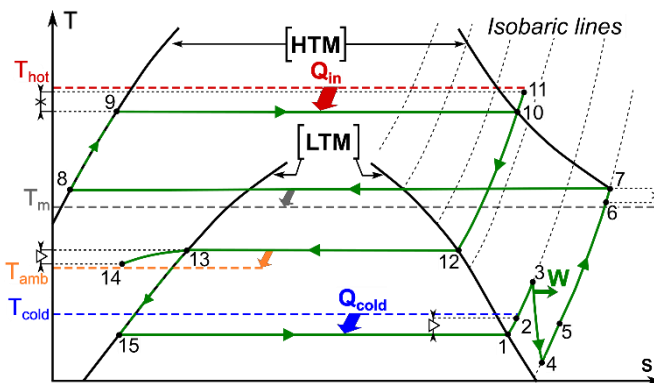


Fig. 6 – Simultaneous power and cold production mode of a hybrid solid/gas chemical reaction cycle: thermodynamic path in the T-s diagram of ammonia (see Fig. 3 for captions).

2.3.c. Combined power and cold production mode: cycle and thermodynamic path

Finally, the pattern of the cycle in **combined** power and cold production mode is given in a Clausius-Clapeyron diagram in Fig. 7, and Fig. 8 adds information on entropy variations within the cycle. This cycle combines the non-isobaric charging step of the separated mode (points 9 to 15) with the non-isobaric discharging step of the simultaneous mode (points 16 to 8), which enables increased total power production (for a given heat input Q_{in}) to $W = W_1 + W_2$. On the other hand, the reactor design in this mode will have to address technical barriers regarding both the high pressure ($P_9 = P_{11} = P_{dec,H}$) and low pressure ($P_4 = P_7 = P_{synth,H}$) of the cycle.

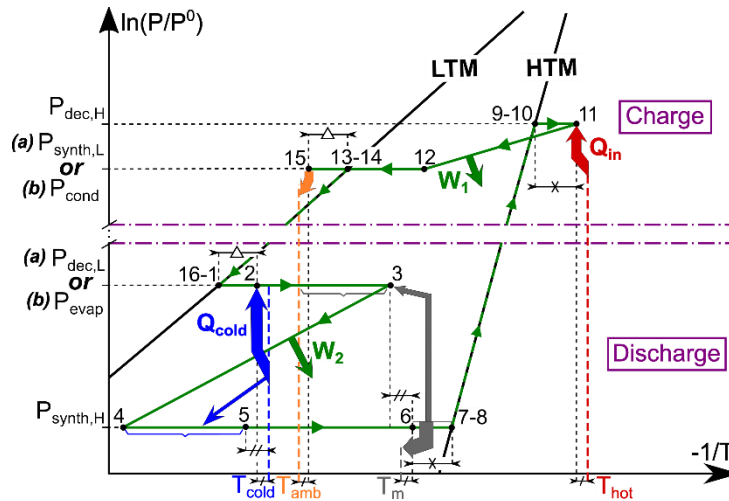


Fig. 7 – Combined power and cold production mode of a hybrid solid/gas chemical reaction cycle: thermodynamic path in a Clausius-Clapeyron diagram (see Fig. 3 for captions).

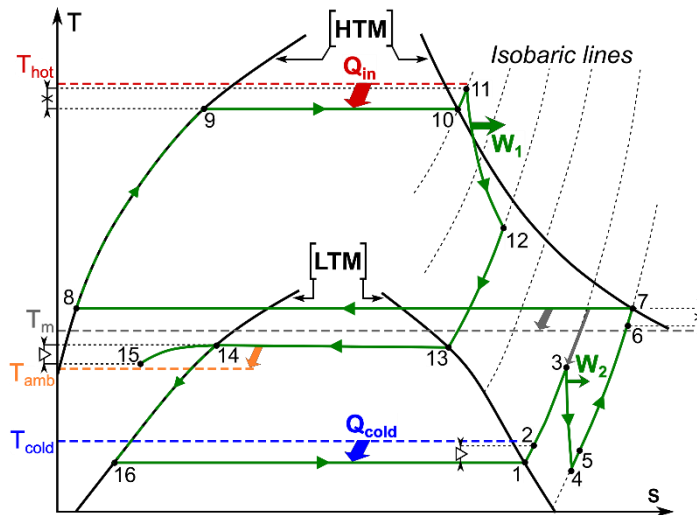


Fig. 8 – Combined power and cold production mode of a hybrid solid/gas chemical reaction cycle: thermodynamic path in the T-s diagram of ammonia (see Fig. 3 for captions).

3. Thermodynamic study

3.1. Model

3.1.a. Thermodynamic and process assumptions

The assumptions for the thermodynamic study are defined below:

- The system has reached a steady state (this assumption is needed for this energy-related study, despite the dynamic behavior of chemical reactions).
- Kinetic and potential energy variations are neglected.
- Heat losses are neglected in all components throughout the cycle.
- Pressure drops are also neglected.
- The reference temperature used in exergy calculations is $T^0 = T_{amb}$.
- For the expander, an isentropic efficiency, η_{is} , is introduced, according to the assumptions of Table 1.
- Different temperature pinches are defined in the process:
 - For (liquid/liquid) or (liquid/vapor) heat exchange: ΔT_{HX1} .
 - For (vapor/vapor) heat exchange: ΔT_{HX2} .
 - For the deviation from thermodynamic equilibrium required for a chemical reaction or a liquid/vapor phase change to proceed, respectively ΔT_{r-eg} and ΔT_{LV-eg} .

This thermodynamic equilibrium deviation has to be taken into account for chemical reactions, but it is not usually rate-limiting for a liquid/vapor phase change, thus $\Delta T_{LV-eg} = 0$ K.

3.1.b. Model equations

As illustrated in Fig. 3 to Fig. 8 and explained in §2.1., the thermodynamic path and other characteristics of hybrid cycle operation can be calculated once the two thermodynamic equilibrium curves are defined (straight lines in Fig. 3, Fig. 5 and Fig. 7; bell-shaped curves in Fig. 4, Fig. 6 and Fig. 8). Each of these thermodynamic equilibria is monovariant, and can be expressed as $P = \Pi(T)$:

$$\text{- For ammonia liquid-vapor equilibrium: } \ln\left(\frac{P}{P^0}\right) = -\frac{L_{vap}}{R.T} + \frac{\Delta S_{vap}}{R} \quad (1)$$

$$\text{- For a chemical reaction equilibrium: } \ln\left(\frac{P}{P^0}\right) = -\frac{\Delta_r H^0}{R.T} + \frac{\Delta_r S^0}{R} \quad (2)$$

The thermodynamic states of the fluid at each point of the cycle are calculated according to the transformations described in §2.3. and Fig. 3 to Fig. 8. Once the thermodynamic path is determined, input and output energies are computed in order to evaluate the cycle performances. Three equations are needed: one for work output, another for heat input, and another for cold production. Each is detailed below for each of the three modes:

- **Separated** power and cold mode (see Fig. 3 and Fig. 4):

$$W = m_{NH3,cycled} \cdot (h_2 - h_3) \quad (3)$$

$$Q_{in} = n_{NH3,cycled} \cdot \Delta_r H(T_1, P_1) + [V_{met,H} \cdot \rho_{met} \cdot c_{met} + n_{HTM} \cdot \bar{C}_{HTM}] \cdot (T_2 - T_{10}) \quad (4)$$

$$Q_{cold} = n_{NH3,cycled} \cdot \Delta_r H(T_8, P_8) - [V_{met,L} \cdot \rho_{met} \cdot c_{met} + n_{LTM} \cdot \bar{C}_{LTM}] \cdot (T_6 - T_9) \quad (5a)$$

$$\text{or } Q_{cold} = n_{NH3,cycled} \cdot L_{vap}(T_8) - m_{NH3,cycled} \cdot (h_5 - h_7) \quad (5b)$$

- **Simultaneous** power and cold production (see Fig. 5 and Fig. 6):

$$W = m_{NH3,cycled} \cdot (h_3 - h_4) \quad (6)$$

$$Q_{in} = n_{NH3,cycled} \cdot \Delta_r H(T_{10}, P_{10}) + [V_{met,H} \cdot \rho_{met} \cdot c_{met} + n_{HTM} \cdot \bar{C}_{HTM}] \cdot (T_{11} - T_6) \quad (7)$$

$$Q_{cold} = n_{NH3,cycled} \cdot \Delta_r H(T_1, P_1) + m_{NH3,cycled} \cdot (h_5 - h_4) - [V_{met,L} \cdot \rho_{met} \cdot c_{met} + n_{LTM} \cdot \bar{C}_{LTM}] \cdot (T_{14} - T_2) \quad (8a)$$

$$\text{or } Q_{cold} = n_{NH3,cycled} \cdot L_{vap}(T_1) + m_{NH3,cycled} \cdot (h_5 - h_4) - m_{NH3,cycled} \cdot (h_{13} - h_{15}) \quad (8b)$$

- **Combined** power and cold production (see Fig. 7 and Fig. 8):

$$W = m_{NH3,cycled} \cdot (h_3 - h_4) + m_{NH3,cycled} \cdot (h_{11} - h_{12}) \quad (9)$$

$$Q_{in} = n_{NH3,cycled} \cdot \Delta_r H(T_{10}, P_{10}) + [V_{met,H} \cdot \rho_{met} \cdot c_{met} + n_{HTM} \cdot \bar{C}_{HTM}] \cdot (T_{11} - T_6) \quad (10)$$

$$Q_{cold} = n_{NH3,cycled} \cdot \Delta_r H(T_1, P_1) + m_{NH3,cycled} \cdot (h_5 - h_4) - [V_{met,L} \cdot \rho_{met} \cdot c_{met} + n_{LTM} \cdot \bar{C}_{LTM}] \cdot (T_{15} - T_2) \quad (11a.)$$

$$\text{or } Q_{cold} = n_{NH3,cycled} \cdot L_{vap}(T_1) + m_{NH3,cycled} \cdot (h_5 - h_4) - m_{NH3,cycled} \cdot (h_{14} - h_{16}) \quad (11b.)$$

where

$$\bar{C}_{HTM} = X_{max} \cdot C_{HTM,r} + (1 - X_{max}) \cdot C_{HTM,p} \quad (12)$$

$$\text{and } \bar{C}_{LTM} = X_{max} \cdot C_{LTM,r} + (1 - X_{max}) \cdot C_{LTM,p} \quad (13)$$

are respectively the molar heat capacities of the High Temperature Material and Low Temperature Material at the end of the synthesis reaction.

Moreover, η_{is} is linked to the cycle points, for example in separated power and cold mode (Fig. 3 and Fig. 4), by:

$$\eta_{is} = (h_3 - h_2) / (h_{3,is} - h_2) \quad (14)$$

For the chemical reactors, three parameters are introduced:

- The range of reaction advancement: $\Delta X = X_{max} - X_{min}$, such that $n_{NH3,cycled} = v_{salt} \cdot \Delta X \cdot n_{salt}$ (15)

- The ratio of wall metal of the reactor to reactive composite volume, $\tau_{met}(-)$, such that: $V_{met} = \tau_{met} \cdot V_{comp}$ (16)

This parameter is related to the thermochemical reactor configuration, and is involved in the sensible heat terms of Eq. (4), (5a.), (7), (8a.), (10) and (11a.).

- The porosity ε of the composite bed implementing the reactive salt in reactors, which is set to 0.7.

This parameter is such that $V_{porous} = \varepsilon \cdot V_{comp}$ and $V_{salt} = (1 - \varepsilon) \cdot V_{comp}$.

Finally, regarding cold production, Q_{cold} , two expressions are given for each mode (respectively (5a.)-(5b.), (8a.)-(8b.) and (11a.)-(11b.)) in order to differentiate between resorption (a.) and single sorption (b.) cycles.

3.1.c. Sets of assumptions for 'perfect' and 'real' cases

For each cycle, two cases are simulated: 'perfect' case for favorable assumptions and 'real' case for unfavorable assumptions: the *perfect* case assumes ideal transformations and gives the maximal performances of the cycle (case usually considered in the previous studies - see §2.2.) while the *real* case sets realistic values for the parameters, based on experience with ORC and thermochemical machines. The two corresponding sets of values for the parameters are reported in Table 1.

Parameters	'Perfect' case	'Real' case
η_{is} (-)	1	0.8
ΔX (-)	1	0.8
τ_{met} (-)	0	0.1
ΔT_{HX1} (K)	0	5
ΔT_{HX2} (K)	0	10
ΔT_{r-eq} (K)	0	20

Table 1 – Values of the main parameters of the model (defined in §3.1.a. and §3.1.b.) for the two simulated cases (ε and ΔT_{LV-eq} are assumed constant)

3.2. Operating conditions and technological boundary values

To study these thermodynamic processes, it is essential to define the main temperature levels in order to set the framework for the performance calculations:

- Focusing on refrigeration, the cold production temperature is set at $T_{cold} = 0^\circ\text{C}$.
- The ambient temperature (heat sink temperature for the release of condensation or synthesis heats) is set at $T_{amb} = 20^\circ\text{C}$.
- Heat source temperature T_{hot} is not fixed but instead results from calculations for a given cycle (see §3.3.). However, a boundary value is set at $T_{hot,max} = 250^\circ\text{C}$ in order to fulfil the target of low-grade heat utilization.

Furthermore, some technological limit values are set for different variables:

- Ammonia pressure is bounded by $P_{min} = 0.1$ bar and $P_{max} = 30$ bar, for technical safety and cost criteria;
- A minimal vapor quality $x_{min} = 0.8$ is required at the expander outlet, in order to avoid damaging it;
- A maximal volumetric ratio $R_{v,max} = 10$ is assumed for expanders, and it complies with the nominal range of scroll expanders, which are particularly targeted and suitable for small facilities. Taking Fig. 3 and Fig. 4 as an example, the volumetric expansion ratio is defined by:

$$R_v = v_3/v_2 \quad (17)$$

3.3. Methodology

The calculation process described hereafter was performed using EES software [28].

This thermodynamic study is based on energy calculations. For the sake of clarity, electrical production at the expander outlet is fixed at $W = 1$ kWh. Then, all other extensive quantities related to one cycle (Q_{in} , Q_{cold} , masses, volumes, ...) are computed, and specific values can then be calculated by ratioing extensive values to the mass of cycled working fluid $m_{NH3,cycled}$.

The purpose of this study is to explore the potential of the hybrid sorption cycles described in §2.3. for different solid reactive salts, and to emerge the most promising reactants. To this end, we use a database of thermochemical data (reaction enthalpy $\Delta_r H^0$ and entropy $\Delta_r S^0$) for 103 reactive ammonia salts. These salts are

mainly metallic chlorides, bromides and iodides, such as CaCl_2 , MnCl_2 , FeBr_2 , or SrI_2 . The database comes from values collected and computed by Touzain [29] and from CNRS-PROMES research. Other available data (molar mass, heat capacity and density of the salts) has been added. Note that at this stage, only a general thermodynamic study is required, so it does not integrate any external issues (such as cost, toxicity, corrosiveness or specific operating characteristics).

First, we set the LTM thermodynamic equilibrium: either a chemical reaction equilibrium (for resorption cycles) or the ammonia liquid–vapor equilibrium (for single sorption cycles). In the next sections, the LTM for resorption is BaCl_2 (8/0) NH_3 , as it enables cold production at target temperature $T_{\text{cold}} = 0^\circ\text{C}$ under a decomposition pressure (see Fig. 3, Fig. 5 and Fig. 7) of $P_{\text{dec,L}} = 0.09$ bar, which is close to the limit value $P_{\text{min}} = 0.1$ bar, and there are no other candidate ammonia salts able to operate at a higher pressure for the same cold production. Note that implementing an expander downstream of the LTM decomposition reactor to generate power is unrealistic due to this low $P_{\text{dec,L}}$ value. Hence the most appropriate configurations for **separated** and **combined** modes have to mobilize ammonia as LTM and its liquid/vapor thermodynamic equilibrium. This means that only the single sorption cycles are studied in §5. (**separated** mode) and §6. (**combined** mode).

Each of the 103 reactive salts is successively selected as HTM, and the thermodynamic path (i.e. pressure, temperature, specific enthalpy and entropy at each key point of the cycle) is computed. Then, the energy amounts Q_{in} (see Eq. (4), (7) and (10)) and Q_{cold} (see Eq. (5), (8) and (11)) are calculated, and relevant variables such as R_v (or $R_{v,1}$ and $R_{v,2}$, when several expansion stages are considered), $m_{\text{NH}_3,\text{cycled}}$ (for $W = 1$ kWh, see Eq. (3), (6) and (9)), $m_{\text{NH}_3,\text{cycled}}$ and T_{hot} are deduced.

Then, in order to pick out the most relevant reactive salts from among the large set databased, five relevant performance criteria are defined and computed for each HTM:

- Energy efficiency

$$\eta_I = \frac{W + Q_{\text{cold}}}{Q_{\text{in}}} \quad (18)$$

- Exergy efficiency

$$\eta_{\text{ex}} = \frac{W + \text{Ex}_{\text{cold}}}{\text{Ex}_{\text{in}}} \quad (19)$$

- Power production ratio

$$\tau_w = \frac{W}{W + Q_{\text{cold}}} \quad (20)$$

- Specific work output

$$w = \frac{W}{m_{\text{NH}_3,\text{cycled}}} \quad (21)$$

- Specific exergy output

$$w + \text{ex}_{\text{cold}} = \frac{W + \text{Ex}_{\text{cold}}}{m_{\text{NH}_3,\text{cycled}}} \quad (22)$$

with

$$\text{Ex}_{\text{in}} = Q_{\text{in}} \cdot \left(1 - \frac{T^0}{T_{\text{hot}}}\right) \quad (23)$$

and

$$\text{Ex}_{\text{cold}} = Q_{\text{cold}} \cdot \left(\frac{T^0}{T_{\text{cold}}} - 1\right) \quad (24)$$

Energy efficiency η_I (Eq. (18)) is the ratio of the total useful energy to input energy, where the useful effects are both work and cold production. This cogeneration efficiency is suitable for comparison with other cogeneration cycles working under the same temperatures (T_{cold} , T_{amb} , T_{hot}).

Nevertheless, it is not possible to run a fair comparison between cogeneration cycles using only the first-law efficiency η_I . Therefore, τ_w (Eq. (20)) represents the part of mechanical work among the two useful effects of the cycle. In addition, in order to take better account of the part of mechanical work produced and the temperature required for the heat source, T_{hot} , the exergy efficiency η_{ex} (Eq. (19)) is computed. It accounts for the differences between work output and heat at several temperature levels, through the Carnot factors which depend on T_{hot} (Eq. (23)) and T_{cold} (Eq. (24)).

Finally, the last two criteria, w (Eq. (21)) and $w + \text{ex}_{\text{cold}}$ (Eq. (22)), are introduced to provide a more quantitative assessment of both useful effects: work generation and useful exergy, respectively, are ratioed to mass unit of the working fluid.

Once the computations have been done for all reactive salts, a first selection is made and hybrid cycles that cannot meet limit values $R_{v,\text{max}}$, x_{min} , P_{min} , P_{max} or $T_{\text{hot},\text{max}}$ defined in §3.2. are excluded. The remaining salts

are ranked according to each of the previous 5 criteria. For each of these criteria, the 10 best salts are selected. At the end of this process, about 15 to 30 usable reactive salts are selected for each mode.

This general approach thus covers all the possibilities offered by existing solid salts, once we have a fixed LTM. The following sections 4, 5 and 6 gather all performance results for the selected salts in the three operating modes, and for the ‘real’ set of parameters (see Table 1).

4. Separated power and cold production mode

As explained in §2.3.a. and depicted in Fig. 3 (Clausius-Clapeyron diagram) and Fig. 4 (T-s diagram), the **separated** power and cold production mode consists in generating power during the charging step, whereas the refrigeration effect is produced during the discharging step.

Following the methodology described in §3.3., once the LTM is set (ammonia or reactive salt $\text{BaCl}_2(8/0)\text{NH}_3$), the 103 solid reactive salts in the database are individually tested with EES software, and the thermodynamic characteristics of the cycles, as well as their performances, are retrieved.

Fig. 9 presents cycle operating conditions (required heat source temperature and volumetric expansion ratio) for each of the salts selected in this mode, for both configurations (i.e. resorption, Fig. 9a., and single sorption, Fig. 9b.). Note that the selected salts are ranked, on the x-axis, by increasing equilibrium temperature at $P = P^0 = 1$ bar.

For resorption cycles (Fig. 9a.), the volumetric expansion ratio R_v remains constant at 4.7 for the first selected salts (from $\text{CaBr}_2(6/2)\text{NH}_3$ to $\text{SrI}_2(6/2)\text{NH}_3$), because the high pressure $P_1 = P_{dec,H}$ is bounded by the maximum value ($P_{dec,H} = P_{max}$). On the other hand, for the last 6 salts, R_v decreases from 4.7 to 2.1 because the maximal heat source temperature $T_{hot,max}$ is reached, and the pressure $P_1 = P_{dec,H}$ consequently decreases. For all reactive salts, the low pressure of the charging step is set at $P_3 = P_{synth,L} = 4.8$ bar, due to the constraint of rejecting synthesis heat at ambient temperature level T_{amb} .

For single sorption cycles (Fig. 9b.), the required heat source temperatures are lower than for resorption cycles, and the volumetric expansion ratio R_v is also frozen (at 2.5) because $P_{dec,H} = P_{max}$. For all reactive salts, the low pressure of the charging step is set at $P_3 = P_{cond} = 10.0$ bar, due to the constraint of rejecting condensation heat at ambient temperature level. Pressure P_{max} is often reached due to the fact that $P_{synth,L}$ and P_{cond} are already relatively high: the available pressure ratio to carry out an expansion stage between P_{max} and $P_{synth,L}$ (or P_{cond}) is low (between 3 and 6.25).

Fig. 10 gathers the performance results (η_l , η_{ex}) in separated power and cold mode for resorption (left side – Fig. 10a.) and single sorption (right side – Fig. 10b.) cycles. This plot highlights the higher range of performances for resorption compared to single sorption cycles: the ranges are respectively [0.37; 0.61] and [0.26; 0.49] for energy efficiencies, and [0.16; 0.28] and [0.13; 0.29] for exergy efficiencies.

Several reasons explain these differences: first, for a given cycled mass of ammonia, the refrigeration effect Q_{cold} is greater for resorption than for single sorption, because the reaction enthalpy of a solid ammonia salt is far greater than the vaporization enthalpy of ammonia ($\Delta_r H^0 \approx 2.L_{vap}$). Moreover, the specific work output w is higher in the resorption cycle, as pressure $P_3 = P_{synth,L}$ (minimal pressure required to reject heat of the exothermal LTM synthesis reaction at ambient sink temperature, see Fig. 3 and Fig. 4) is lower than P_{cond} (minimal pressure required to reject heat of the exothermal ammonia condensation). This is due to the respective positions of the ammonia liquid–vapor equilibrium curve and sorption equilibrium curve of the LTM used in resorption cycles, $\text{BaCl}_2(8/0)$. Exergy efficiencies follow a similar trend (with lower values for single sorption cycles) but the differences are lower because the heat source temperatures are higher for resorption cycles, as Fig. 9 shows: [212; 250°C] for resorption (Fig. 9a.) against [138; 250°C] for single sorption (Fig. 9b.).

In addition to Fig. 10, Table 2a. and Table 2b. give an overview of the differences between ‘real’ and ‘perfect’ efficiencies (corresponding to the sets of assumptions listed in Table 1): minimal, maximal and mean values are provided for the absolute deviations ($\eta_l - \eta_{l,perfect}$) and ($\eta_{ex} - \eta_{ex,perfect}$), as well as for the relative deviations $(\eta_l - \eta_{l,perfect})/\eta_{l,perfect}$ and $(\eta_{ex} - \eta_{ex,perfect})/\eta_{ex,perfect}$. These tables show a significant drop in energy efficiency (relative deviations reach -37.5% in resorption and -30.5% in single sorption) and even more in exergy efficiency (maximal relative deviations: -57.6% in resorption, -45.3% in single sorption).

From perfect to real case, various parameters are modified (see Table 1), of which the most influential for cycle performances are τ_{met} and ΔT_{r-eq} : the first one increases sensible heat in Q_{in} (Eq. (4)) and Q_{cold} (Eq. (5)), while the second one strongly modifies cycle temperatures, in particular temperature differences ($T_2 - T_{10}$) and ($T_6 - T_9$) which affect Q_{in} and Q_{cold} , respectively

However, some other parameters related to each salt can also explain the performance gap when switching from perfect to real case. From the equations Eq. (3) to (5) (providing detailed expressions of the input and output energies), a development of the expressions of η_I (Eq. (18)) and η_{ex} (Eq. (19)) shows that the factors driving the gap between ‘perfect’ and ‘real’ efficiencies are heat capacities \bar{C}_{HTM} and \bar{C}_{LTM} , reaction stoichiometry (ν_H, ν_L), reaction enthalpy ($\Delta_r H_{HTM}^0, \Delta_r H_{LTM}^0$), density of reactive salts (ρ_{HTM}, ρ_{LTM}) and operating parameters $\eta_{is}, \Delta X, \Delta T_{HX1}, \Delta T_{r-eq}$.

Alongside the dimensionless efficiencies of Fig. 10, useful effects (cold and power production) are detailed in Fig. 11 by means of two specific quantities: w and $w + eX_{cold}$. Note that these values are ratioed to the total mass of ammonia involved in one complete cycle, $m_{NH3,cycled}$ (see Eq. (21) and (22)).

The overview of useful effects given by Fig. 11 supports the previous observations on performances: indeed, work output (green bars) and refrigeration output (included in blue bars) are much higher for resorption than for single sorption cycles. Specific work output w ranges from 161 to 296 kJ/kg_{NH3} for resorption, and from 139 to 190 kJ/kg_{NH3} for single sorption.

However, the power production ratio τ_w (red points and right axis) appears to be slightly lower for resorption ([7.2; 12.5 %]) than single sorption cycles ([10.9; 14.3 %]). This is one of the reasons for the low exergy efficiency differences between resorption and single sorption cycles.

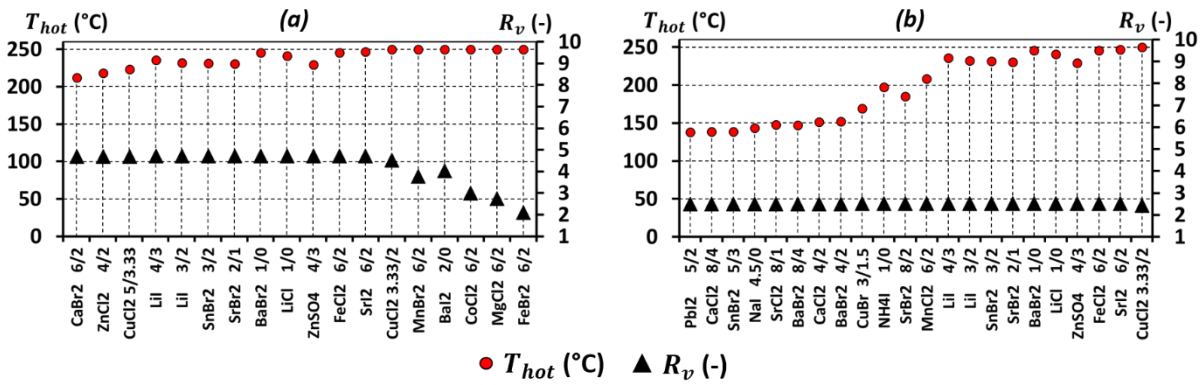


Fig. 9 – Separated power and cold mode: operating conditions of the hybrid cycle for selected salts

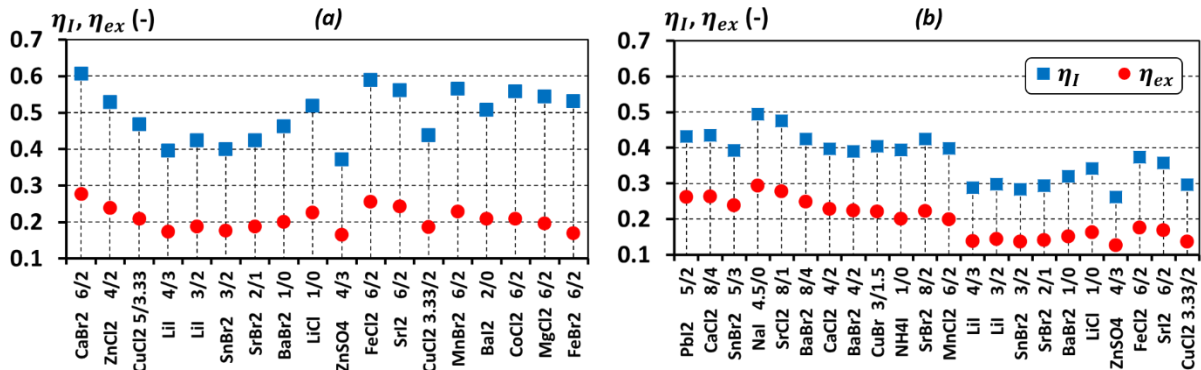


Fig. 10 – Separated power and cold mode: energy and exergy efficiencies of the hybrid cycle for selected salts

(a) Resorption		Mean value	Max. value	Min. value	CaBr ₂ (6/2)NH ₃
η_I	Absolute deviation	- 0.19	- 0.27	- 0.15	- 0.16
	Relative deviation	- 28.4 %	- 37.5 %	- 20.5 %	- 20.6 %
η_{ex}	Absolute deviation	- 0.19	- 0.23	- 0.17	- 0.18
	Relative deviation	- 47.6 %	- 57.6 %	- 39.2 %	- 39.2 %

Table 2a – Separated power and cold mode (resorption): comparison between ‘perfect’ and ‘real’ efficiencies.

- Absolute deviations: $\eta_I - \eta_{I,perfect}$ and $\eta_{ex} - \eta_{ex,perfect}$

- Relative deviations: $(\eta_I - \eta_{I,perfect})/\eta_{I,perfect}$ and $(\eta_{ex} - \eta_{ex,perfect})/\eta_{ex,perfect}$

(b) Single sorption		Mean value	Max. value	Min. value	SrCl ₂ (8/1)NH ₃
η_I	Absolute deviation	- 0.09	- 0.17	- 0.06	- 0.07
	Relative deviation	- 20.2%	- 30.5%	- 13.1%	- 13.1%
η_{ex}	Absolute deviation	- 0.12	- 0.17	- 0.08	- 0.15
	Relative deviation	- 37.9%	- 45.3%	- 31.4%	- 34.7%

Table 2b – Separated power and cold mode (single sorption): comparison between ‘perfect’ and ‘real’ efficiencies

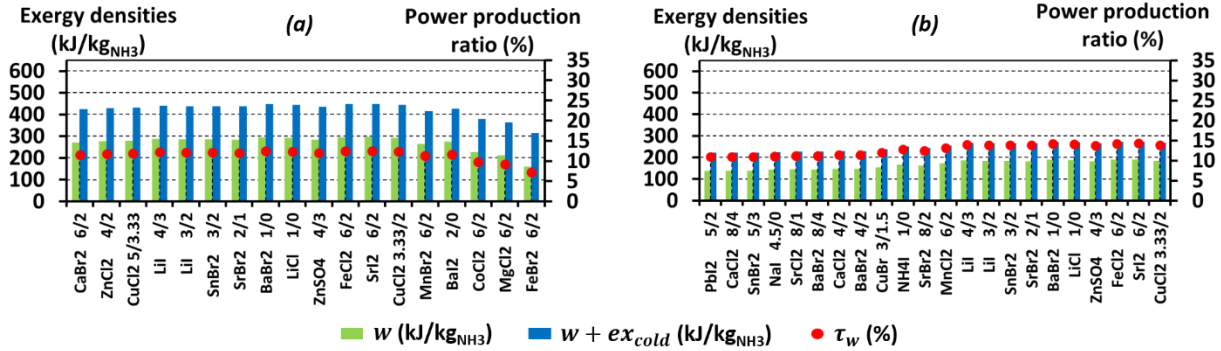


Fig. 11 – Separated power and cold mode: exergy densities and power production ratio

5. Simultaneous power and cold production

This section addresses an innovative cycle configuration in which both cold and mechanical work are produced during the discharging step (step 2 on Fig. 2). In this case, the evaporator is located upstream of the expander, and it also produces the refrigeration effect by operating at a relatively low pressure (due to the LTM equilibrium). Hence the expander works at a lower pressure in this mode than in the previous mode. Only the single sorption cycle is studied in this section, for the reasons stated in §3.3.

The pattern of the hybrid cycle in simultaneous mode is plotted in thermodynamic diagrams in §2.3.b. (Fig. 5 and Fig. 6). However, when volumetric expansion ratio between $P_1 = P_{evap}$ and $P_4 = P_{synth,H}$ is too high (i.e. $R_v > R_{v,max}$), we can implement two expansion stages: more details on this configuration are given in Appendix A.

As in §4.2, five performance criteria are used to pick out the most relevant reactive salts: η_I , η_{ex} , w , τ_w and $w+ex_{cold}$.

First, the operating conditions (heat source temperatures and volumetric expansion ratios) are plotted in Fig. 12. (similar to Fig. 9). The reactive salts flagged ‘*’ require a configuration with two expanders to fulfil the boundary value $R_{v,max} = 10$, while the other salts have been implemented in single expander configurations. The range of heat source temperatures is wider than for separated power and cold mode: [107; 245°C]. Indeed, as the charging step is isobaric, there is no need to aim for higher HTM decomposition pressure and temperature. Furthermore, starting from the salt FeCl₂ (6/2)NH₃, volumetric expansion ratios are frozen at $R_{v,1} \approx R_{v,2} \approx 4.3$, because the pressure $P_4 = P_{synth,H}$ has reached P_{min} .

Fig. 13 gathers the performances (η_I , η_{ex}) for the simultaneous power and cold production mode. As in Fig. 10, only real cases are plotted, and Table 3 is added to give an overview of the performance differences between perfect and real cases.

The energy efficiency η_I is of the same order of magnitude as for the separated mode and single sorption (Fig. 10b.), and ranges from 0.25 to 0.48. This is consistent with the fact that both results relate to single sorption cycles: for both cycles, the refrigeration effect Q_{cold} is mainly due to the vaporization enthalpy of ammonia L_{vap} .

Regarding exergy aspects, the performances are better for the simultaneous power and cold mode than for the separated mode: as Fig. 13 shows, η_{ex} ranges from 0.18 to 0.34. This results from the high values of specific work output w , at a maximum of 399 kJ/kg_{NH3}, and power production ratio τ_w , at a maximum of 25% (Fig. 14), both of which are much higher values than for the separated mode (see §4.). This mode allows a higher power output because it uses a higher pressure difference at the expander boundaries, i.e. between $P_3 = P_{evap}$

and $P_4 = P_{synth,H}$ in Fig. 5. Indeed, the evaporation pressure required to produce cold at $T_{cold} = 0^\circ\text{C}$ is approximately 3.5 bar, while the minimal achievable pressure is set at $P_{min} = 0.1$ bar.

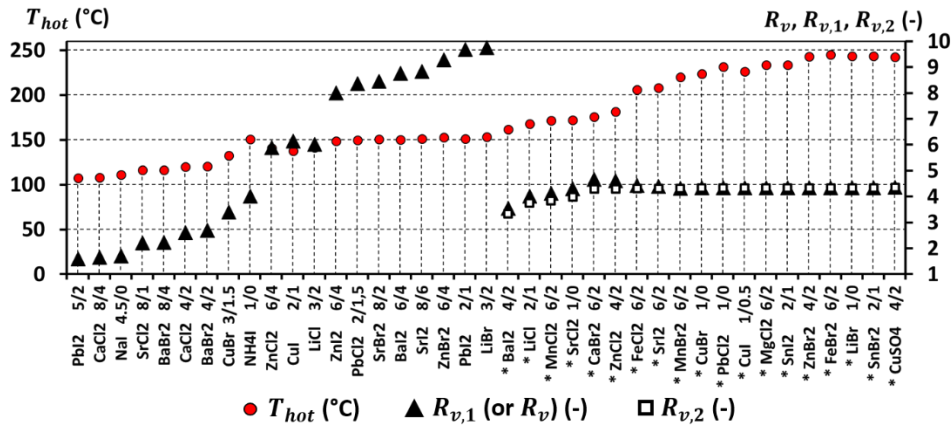


Fig. 12 – Simultaneous power and cold mode: operating conditions of the hybrid cycle for selected salts
*: 2-expansions configuration

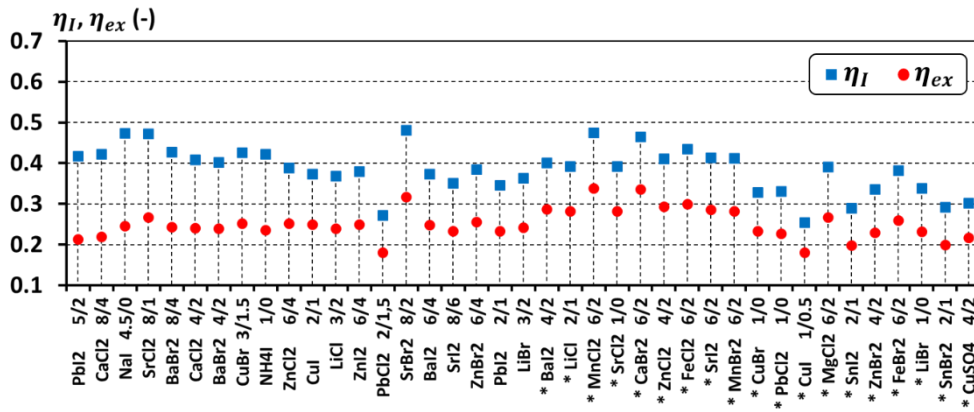


Fig. 13 – Simultaneous power and cold mode: energy and exergy efficiencies of the hybrid cycle for selected salts

		Mean value	Max. value	Min. value	SrCl ₂ (8/1)NH ₃
η_I	Absolute deviation	- 0.15	- 0.25	- 0.10	- 0.18
	Relative deviation	- 28.4 %	- 38.8 %	- 20.0 %	- 27.4 %
η_{ex}	Absolute deviation	- 0.30	- 0.55	- 0.14	- 0.51
	Relative deviation	- 52.5 %	- 72.2 %	- 38.3 %	- 65.7 %

Table 3 – Simultaneous power and cold mode: comparison between ‘perfect’ and ‘real’ efficiencies

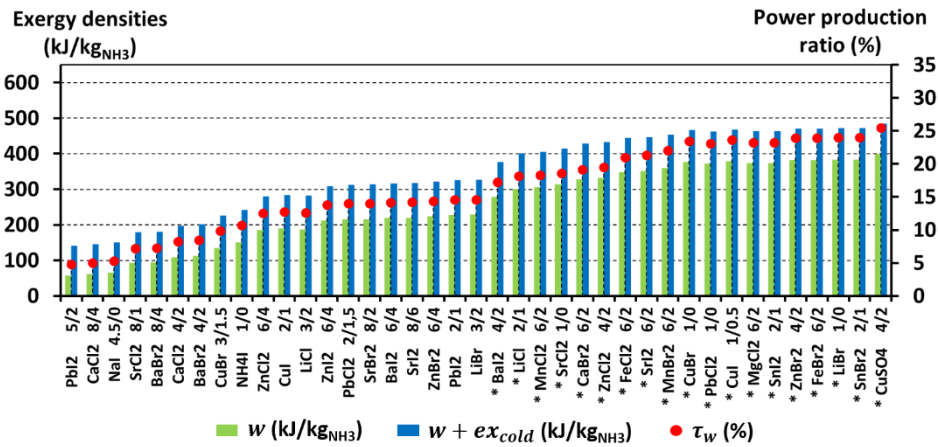


Fig. 14 – Simultaneous power and cold mode: exergy densities and power production ratio

6. Combined mode

Combining the non-isobaric steps of the two previous modes (separated power and cold production mode and simultaneous mode) leads to the cycle presented in Fig. 7 and Fig. 8, in which both the charging and discharging steps produce power. Again, for reasons set out in §3.3., only the single sorption cycle is studied here; a configuration using 2 expansion stages is also considered for some reactive salts (see Appendix A for more details on this configuration).

Firstly, Fig. 15 shows that the range of usable heat source temperatures is the same as for separated power and cold mode in single sorption ([138; 250°C]) but narrower than for simultaneous mode ([107; 245°C]). This is due to the use of the same non-isobaric charging step as in separated mode.

Regarding the useful effects of the cycle, Fig. 17 shows that τ_w ranges from 14.6 to 30.1%, which is higher than all previous cycles. Inserting an expander in both operating steps obviously produces more power, which is highlighted by the high values of specific work output w (from 197 to 547 kJ/kg_{NH3}).

Consequently, the exergy efficiencies are higher in combined power and cold mode than all other cycles: η_{ex} ranges from 0.20 to 0.41 (see Fig. 16). These high values reflect a higher exergy content in the outputs (produced useful effects).

The energy efficiency η_l ranges from 0.26 to 0.51: these are the best values for a single sorption cycle. Only the resorption cycle exceeds these values because of the higher cold production (see Fig. 10a., §4.).

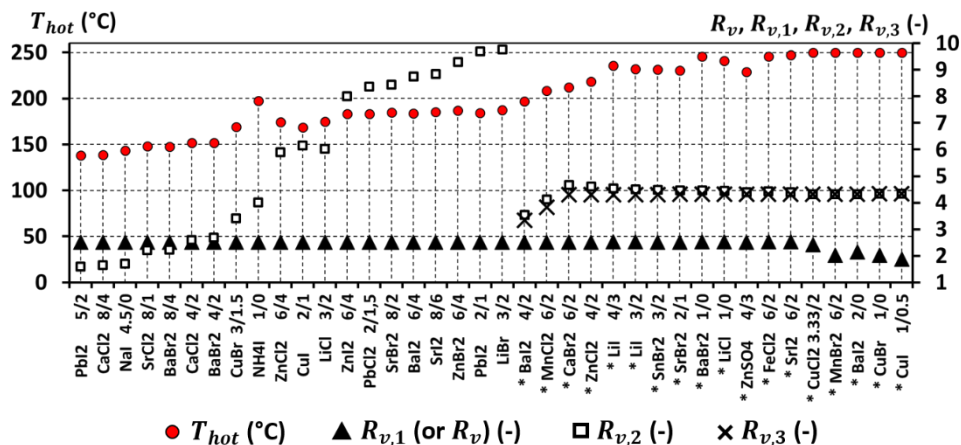


Fig. 15 – Combined power and cold mode: operating conditions of the hybrid cycle for selected salts

*: 2-expansions configuration

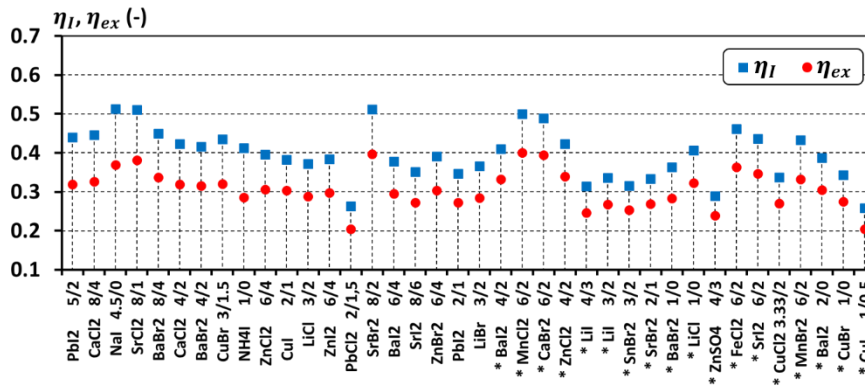


Fig. 16 – Combined power and cold mode: energy and exergy efficiencies of the hybrid cycle for selected salts

		Mean value	Max. value	Min. value	SrCl ₂ (8/1)/NH ₃
η_I	Absolute deviation	- 0.17	- 0.27	- 0.12	- 0.20
	Relative deviation	- 29.7%	- 39.4%	- 21.3%	- 27.7%
η_{ex}	Absolute deviation	- 0.28	- 0.46	- 0.18	- 0.44
	Relative deviation	- 47.5%	- 58.9%	- 36.5%	- 53.4%

Table 4 – Combined power and cold mode: comparison between ‘perfect’ and ‘real’ efficiencies

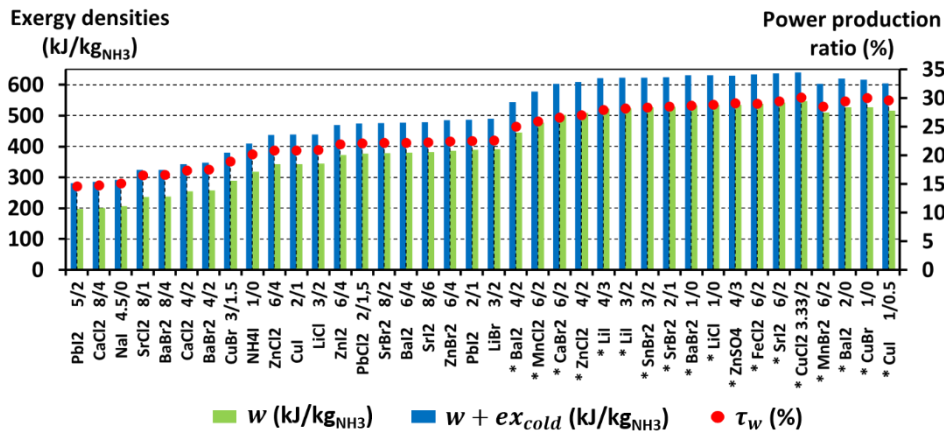


Fig. 17 – Combined power and cold mode: exergy densities and power production ratio

7. Discussion of the results

7.1. Sensitivity of the results to key parameters

7.1.a. Methodology

We ran a sensitivity analysis on the ‘real’ case results taken as nominal case. *Table 1* lists the nominal values of the main parameters, and the variation ranges were chosen in such a way as to keep the extreme values of the parameters realistic. Moreover, the sensitivity study was carried out on combined power and cold mode as it emerged as the most relevant and general mode. The six parameters listed below seem particularly relevant for this study as potential control parameters:

- The following three parameters affect the expansion stages, and the specific work output w :
 - the technological boundary value P_{min} is varied from 0.1 to 1 bar, which may limit the expansion in discharging step.
 - the limit value P_{max} is varied between 30 and 100 bar, which defines an upper limit for the expansion in charging step.

- the isentropic efficiency η_{is} (see Eq. (14)) is varied from 0.7 to 0.9.
- The metal ratio τ_{met} (see Eq. (16)) is varied from 0 to 0.3. This parameter mainly affects efficiencies η_I and η_{ex} , through the sensible heat terms in Q_{in} and Q_{cold} .
- The following two parameters affect temperatures and pressures of the points of the cycle:
 - ΔT_{r-eq} (i.e. the temperature deviation from the chemical reaction equilibrium) is varied between 10 and 40 K, which changes the thermodynamic states of points 3 to 12 on Fig. 7 and Fig. 8, and thus affects specific work output w and exergy.
 - T_{amb} is varied from 15 °C to 25°C, which also modifies the thermodynamic path of the cycle.

7.1.b. Results

The results are presented on Fig. 18 for 3 representative salts: CaCl_2 (8/4) NH_3 , SrCl_2 (8/1) NH_3 and SrBr_2 (8/2) NH_3 . For each salt and each of the 6 parameters, we evaluated the sensitivity of two performance criteria: energy efficiency η_I (red lines) and specific exergy output $w+ex_{cold}$ (green dotted lines). The rationale for choosing these criteria is that they give a good qualitative and quantitative overview of the cycle performances. Sensitivities are plotted as relative deviations with respect to nominal value of the variable: $\Delta(\eta_I)/\eta_{I,nom}$ and $\Delta(w+ex_{cold})/(w+ex_{cold})_{nom}$. Symbols (respectively red filled and green empty symbols) flag extreme deviations.

From this graphical representation, several observations can be made:

- Most of the results fall between -10 and +10% (especially for parameters τ_{met} , η_{is} and T_{amb}).
- Concerning the technological boundary value P_{max} , the specific exergy output $w+ex_{cold}$ is very sensitive to this parameter with all three salts, due to the ceiling effect it has on the thermodynamic path of the cycle: the potential improvement ranges from 26.2 % to 29.7 % according to the salt.
- P_{min} can prove influential depending on the reactive salt: in this example, only the SrBr_2 (8/2) NH_3 cycle has lower performances when P_{min} is set at higher values than the nominal value 0.1 bar (-21.6 % for $w+ex_{cold}$). The reason is that the SrBr_2 (8/2) NH_3 nominal low pressure is $P_4 = P_{synth,H} = 0.3$ bar, which is close to the limit value, whereas $P_{synth,H}$ values for CaCl_2 (8/4) NH_3 and SrCl_2 (8/1) NH_3 , are 1.9 and 1.4 bar, respectively, i.e. far from P_{min} .
- The most influential operating parameter is ΔT_{r-eq} , as it leads to a relative variation range of [-26.1; 15.8%] for $w+ex_{cold}$. This is due to the fact that it changes the thermodynamic path. There is huge potential for improving this parameter if heat transfer is correctly managed. However, a dynamic study is needed for this point.

Finally, note that η_I (red lines and symbols) is less sensitive to the studied parameters than $w+ex_{cold}$, with relative deviations ranging from -13.2 % to 9.3 %. η_I is an energy ratio while $w+ex_{cold}$ is an exergy-related criterion, and the chosen parameters have a more direct influence on operating temperatures and pressures than energy content.

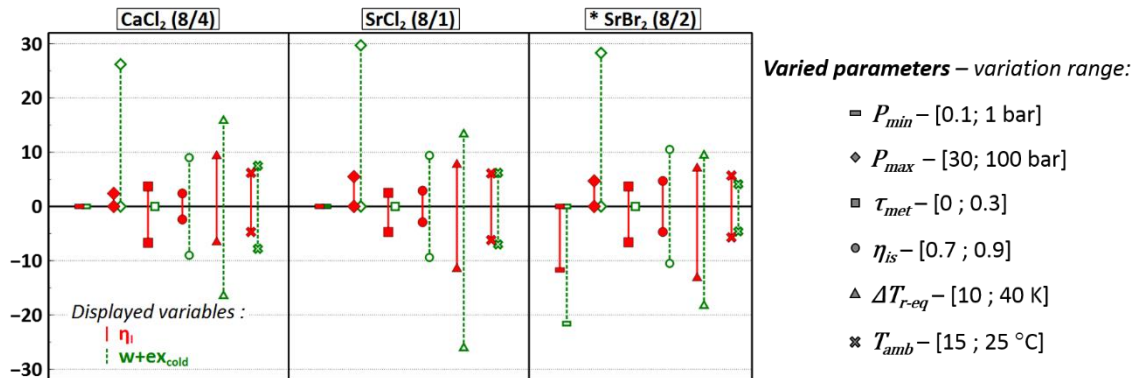


Fig. 18 — Sensitivity analysis for combined power and cold production mode.

Symbols are the extremal relative deviations of η_I and $w+ex_{cold}$ with respect to their nominal values.

7.2. Summary of the results

The main performance criteria for all selected salts from sections 4, 5 and 6 are collected as a function of the cycle regeneration temperature T_{hot} on Figs. 19 to 21. These plots serve to discriminate between the three studied modes for achieving effective cogeneration of power and cold for a given heat source:

- The resorption cycle in separated power and cold mode (green triangles) cannot be run with a heat source temperature under 212°C. It provides higher energy efficiency than the other cycles ([0.34; 0.61], see Fig. 19) due to its high cold production, but its exergy efficiency is lower than the simultaneous and combined modes ([0.13; 0.30], see Fig. 20) due to its low power production ratio. Finally, in relation to the high cold production but low power production ratio, the specific exergy output $w+ex_{cold}$ (see Fig. 21) lies between the single sorption cycle in separated mode and the two other modes.
- The single sorption cycle in separated mode (blue triangles) is suitable for using a lower-temperature heat source, as it requires a heat source temperature higher than 138°C. However, despite a comparable power output, it provides a lower cold output than the resorption cycle, thus underperforms on energy efficiency ([0.24; 0.49], see Fig. 19) and exergy efficiency ([0.06; 0.29], see Fig. 20).
- The simultaneous power and cold mode (black squares) is relevant for the low-temperature sources, as the minimal required regeneration temperature T_{hot} is only 107°C. Its energy efficiency is enormously dependent on the reactive salt used, and lies within the range [0.25; 0.54] (see Fig. 19), i.e. lower values than for the resorption cycle in separated mode (due to the higher cold production of resorption cycle). Its higher power production ratio means that exergy efficiency and specific exergy output are higher than for the two previous cycles (exergy efficiency range is [0.18; 0.34], see Fig. 20).
- The charging step of the combined mode (red circles) is the same as for the single sorption cycle in separated mode, so they share the same required heat source temperature. The energy efficiency ([0.26; 0.51], see Fig. 19) is higher than for simultaneous mode and for the single sorption cycle in separated mode, but remains lower than for the resorption cycle in separated mode which offers higher cold production; furthermore, driven by the higher exergy content of the outputs (higher power production ratio), this cycle presents the highest exergy efficiency ([0.20; 0.40], see Fig. 20) and specific exergy output ([281; 640 kJ/kg_{NH₃}], see Fig. 21).

At 30 °C to 400 °C heat source temperatures, energy efficiencies of existing hybrid thermochemical cycles (detailed in §2.2.) lie in the range [0.06; 0.62], while exergy efficiencies are in the range [0.12; 0.90]. Here, heat source temperatures ranged from 107 °C to 250 °C, energy efficiencies from 0.24 to 0.61 and exergy efficiencies from 0.06 to 0.40. However, we cannot offer a fair comparison, as different studies have used different sets of assumptions and operating conditions (cold production temperatures, heat sink temperatures, etc.).

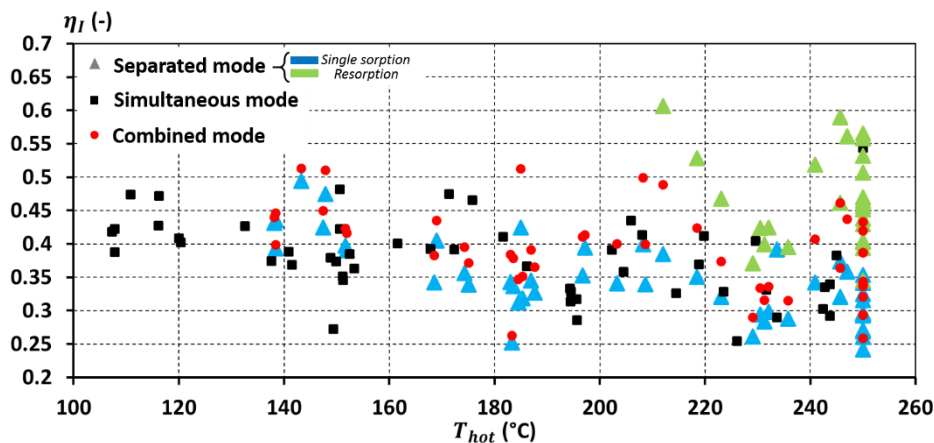


Fig. 19 – Energy efficiencies: summary of all selected salts in the 3 cogeneration modes

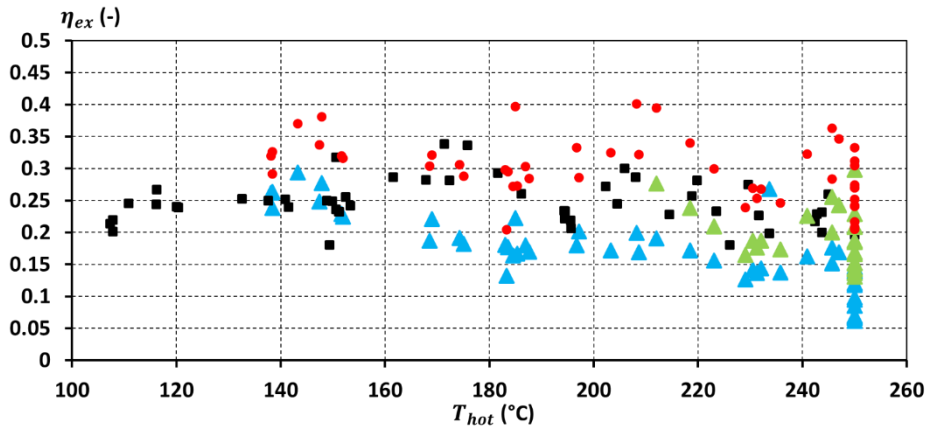


Fig. 20 – Exergy efficiencies: summary of all selected salts in the 3 cogeneration modes

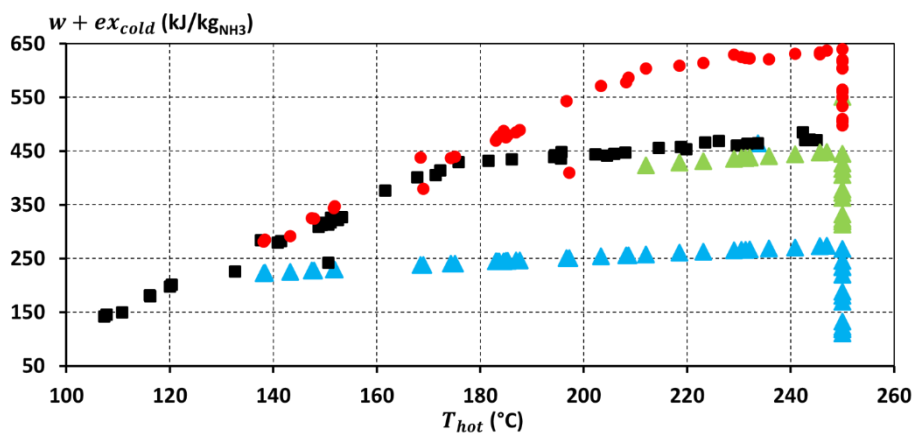


Fig. 21 – Specific exergy output: summary of all selected salts in the 3 cogeneration modes

To conclude our analysis of a number of criteria describing operating conditions and performances, the advantages and possible applications of each cycle are charted in Fig. 22. It should be underlined that these three hybrid configurations can meet different demands and applications depending on the available heat source temperature and/or the share of mechanical work needed.

Characteristics :	Separated mode		Simultaneous mode	Combined mode
	Resorption cycle	Single sorption cycle		
Valorization of low-grade waste heat	$T_{hot} > 212^{\circ} C$	$T_{hot} > 138^{\circ} C$	$T_{hot} > 107^{\circ} C$	$T_{hot} > 138^{\circ} C$
Proportion of power production	$7.2 < \tau_w < 12.5 \%$	$10.9 < \tau_w < 14.3 \%$	$4.8 < \tau_w < 25.5 \%$	$14.6 < \tau_w < 30.1 \%$
Storage of the cold production				
Storage of the power production				
Specific exergy output (kJ/kg _{NH3})	$313 < w + ex_{cold} < 448$	$110 < w + ex_{cold} < 464$	$142 < w + ex_{cold} < 485$	$281 < w + ex_{cold} < 640$

Performance level: ■ Good ■ Average ■ Weak

Figure 22 – Overview of the strengths and weaknesses of each mode

8. Conclusions

This paper investigated three ways of hybridizing the solid/gas sorption cycles with the power cycle, leading to three operating modes for power and cold cogeneration with a storage function of either cold or cold

and power. The potential of these three modes was explored using an innovative methodology to select the most promising reactive salts for each mode.

The energy efficiencies of the proposed hybrid cycles ranged from 0.24 to 0.61, the highest values being reached for the resorption cycle in separated mode. Exergy efficiencies ranged from 0.06 to 0.40, and the best values were obtained in combined mode, due to its high power production ratios. Note that the innovative simultaneous and combined modes emerge as promising developments for applications where a power storage is required. In comparison with the separated mode, they offer particularly high power production ratios (the maximal value is 30.1%) and exergy densities (the maximal value is 640 kJ/kg_{NH₃}).

Note too that these hybrid thermochemical cycles can also focus on energy storage and power production. In such case, during the discharging step, the temperature of the LTM vapor generator is no longer set at T_{cold} and so an *auto-thermal* system can be performed in this step (see Fig. 2) by recovering the surplus heat of the exothermal vapor absorption (Q_m) to achieve the endothermal vapor generation upstream of the expander. This leads to several other configurations that have also been the subject of a thermodynamic study, with results that will be presented in a separate paper.

Building on this first study, the next step is to analyze the dynamic behavior of the cycles, where the coupling between the chemical reactor and the expander appears to pose a number of challenges: indeed, antagonistic purposes have to be achieved in order to simultaneously improve both chemical reaction kinetics and power generation at the expander. For example, on Fig. 5 and Fig. 7 (in the discharging step):

- Improving chemical reaction kinetics for the HTM synthesis reaction entails increasing the temperature gap between ammonia vapor coming from the expander (point 6) and the thermodynamic equilibrium of the reaction (points 7-8). If temperature T_m is fixed, this must be achieved by increasing the low pressure $P_4 = P_{synth,H}$.
- Improving power generation entails increasing the pressure difference between the inlet (point 3) and outlet of the expander (point 4). Since pressure P_3 is fixed, this must be achieved by reducing pressure $P_4 = P_{synth,H}$.

For the dynamic study, discussion should revolve around choosing one solid reactant, and the criteria considered should go beyond performances to encompass factors such as the toxicity, corrosiveness and/or cost of the salts.

Finally, an experimental setup will be required to validate the theoretical predictions and assess the feasibility of such hybrid thermochemical cycles. Monitoring the changes in pressure and mass flow rate conditions during operation of this machine will be of great importance to validate the above-mentioned dynamic study of the coupling between expander and chemical reactor. The design of a prototype is in progress, and a scroll expander is already available and operable with ammonia and under the predicted temperature and pressure conditions.

Acknowledgements

The authors thank Pierre Neveu for his invaluable support in thermodynamics. Alexis Godefroy was supported by a PhD grant from the French Ministry of National Education (doctoral contract #2017-09-ED.305).

References

- [1] Ammar Y, Joyce S, Norman R, Wang Y, Roskilly AP. Low grade thermal energy sources and uses from the process industry in the UK. *Applied Energy* 2012;89:3-20.
- [2] Ling-Chin J, Bao H, Ma Z, Taylor W, Roskilly AP. (2019). State-of-the-Art Technologies on Low-Grade Heat Recovery and Utilization in Industry. In: Al-Bahadly IH, editor. *Energy Conversion: Current Technologies and Future Trends*; 2018, p. 55-73.
- [3] Stutz B, Le Pierrès N, Kuznik F, Johannes K, Palomo del Barrio E, Bedecarrats JP, et al. Storage of thermal solar energy. *Comptes Rendus Physique* 2017;18:401-14.
- [4] Nadeem F, Hussain S, Tiwari P, Goswami AK, Ustun TS. Comparative Review of Energy Storage Systems, Their Roles, and Impacts on Future Power Systems. *IEEE Access* 2019;7:4555-85.

- [5] Srihirin P, Aphornratana S, Chungpaibulpatana S. A review of absorption refrigeration technologies. *Renewable and Sustainable Energy Reviews* 2001;5:343-72.
- [6] Elsheniti MB, Elsamni OA, Al-dadah RK, Mahmoud S, Elsayed E, Saleh K. Adsorption refrigeration technologies. In: Ghenai C, Salameh T, editors. *Sustainable Air Conditioning Systems*; 2018, p. 71-95.
- [7] Xu F, Goswami DY, Bhagwat SS. A combined power / cooling cycle. *Energy* 2000;25:233-46.
- [8] Tamm G, Goswami DY, Lu S, Hasan AA. Theoretical and experimental investigation of an ammonia-water power and refrigeration thermodynamic cycle. *Solar Energy* 2004;76:217-28.
- [9] Wang L, Ziegler F, Roskilly AP, Wang R, Wang Y. A resorption cycle for the cogeneration of electricity and refrigeration. *Applied Energy* 2013;106:56-64.
- [10] Jiang L, Roskilly AP, Wang RZ, Wang LW. Analysis on innovative resorption cycle for power and refrigeration cogeneration. *Applied Energy* 2018;218:10-21.
- [11] Jiang L, Wang LW, Liu CZ, Wang RZ. Experimental study on a resorption system for power and refrigeration cogeneration. *Energy* 2016;97:182-90.
- [12] Hasan AA, Goswami DY, Vijayaraghavan S. First and second law analysis of a new power and refrigeration thermodynamic cycle using a solar heat source. *Solar Energy* 2002;73:385-93.
- [13] Ayou DS, Bruno JC, Saravanan R, Coronas A. An overview of combined absorption power and cooling cycles. *Renewable and Sustainable Energy Reviews* 2013;21:728-48.
- [14] Ventas R, Lecuona A, Vereda C, Rodriguez-Hidalgo MC. Performance analysis of an absorption double-effect cycle for power and cold generation using ammonia/lithium nitrate. *Applied Thermal Engineering* 2017;115:256-66.
- [15] Ziegler F, Jahnke A, Karow M. Re-evaluation of the Honigmann-process: thermo-chemical heat store for the supply of electricity and refrigeration. *Vortrag und Proc. of the Heat Powered Cycles Conference, Berlin, 2009.*
- [16] Ziegler F, Jahnke A, Strenge L, Flessner C, Wolf N, Jungnickel T. First cycle simulations of the Honigmann process with LiBr / H₂O and NaOH / H₂O as working fluid pairs as a thermochemical energy storage. *International Journal of Low-Carbon Technologies* 2013;8:155-61.
- [17] Bao H, Ma Z, Roskilly AP. Integrated chemisorption cycles for ultra-low grade heat recovery and thermo-electric energy storage and exploitation. *Applied Energy* 2016;164:228-36.
- [18] Bao H, Ma Z, Roskilly AP. Chemisorption power generation driven by low grade heat – Theoretical analysis and comparison with pumpless ORC. *Applied Energy* 2017;186:282-90.
- [19] Bao H, Ma Z, Roskilly AP. A chemisorption power generation cycle with multi-stage expansion driven by low grade heat. *Energy Conversion and Management* 2017;150:956-65.
- [20] Lu Y, Roskilly AP, Wang Y, Wang L. Study of a novel dual-source chemisorption power generation system using scroll expander. *Energy Procedia* 2017;105:921-6.
- [21] Lu Y, Roskilly AP, Tang K, Wang Y, Jiang L, Yuan Y, et al. Investigation and performance study of a dual-source chemisorption power generation cycle using scroll expander. *Applied Energy* 2017;204:979-93.
- [22] Jiang L, Lu YJ, Roskilly AP, Wang RZ, Wang LW, Tang K. Exploration of ammonia resorption cycle for power generation by using novel composite sorbent. *Applied Energy* 2018;215:457-67.
- [23] Jiang L, Wang LW, Zhang XF, Liu CZ, Wang RZ. Performance prediction on a resorption cogeneration cycle for power and refrigeration with energy storage. *Renewable Energy* 2015;83:1250-9.

[24] Lu Y, Wang Y, Bao H, Yuan Y, Wang L, Roskilly AP. Analysis of an optimal resorption cogeneration using mass and heat recovery processes. *Applied Energy* 2015;160:892-901.

[25] Bao H, Wang Y, Roskilly AP. Modelling of a chemisorption refrigeration and power cogeneration system. *Applied Energy* 2014;119:351-62.

[26] Bao H, Wang Y, Charamboulos C, Lu Z, Wang L, Wang R, et al. Chemisorption cooling and electric power cogeneration system driven by low grade heat. *Energy* 2014;72:590-8.

[27] Neveu P, Domblides JP, Castaing-Lasvignottes J. Diagrammes thermodynamiques relatifs aux équilibres solide / gaz. *Proceedings of the International Ab-sorption HTP Conference, Montréal, 1996:237-44.*

[28] F-Chart Software : Engineering Software EES: Engineering Equation Solver <http://www.fchart.com/ees/>.

[29] Touzain P. Thermodynamic values of ammonia-salts reactions for chemical sorption heat pumps. *Proceedings of the International Sorption Heat Pump Conference, Munich, 1999:225-38.*

Appendix A. Configurations with two expansion stages (simultaneous and combined modes)

As stated in §5. and §6., we investigated configurations using two expansion stages in the discharging step for the simultaneous and combined modes, and for selected reactive salts. To complement the drawings of §2.3.b. and §2.3.c., these configurations are depicted in *Fig. A1* to *A4* (using Clausius-Clapeyron and T-s diagrams). Moreover, similar to §3.1.b., the expressions of input and output energies for these cycles are given by Eq. (A1) to (A6).

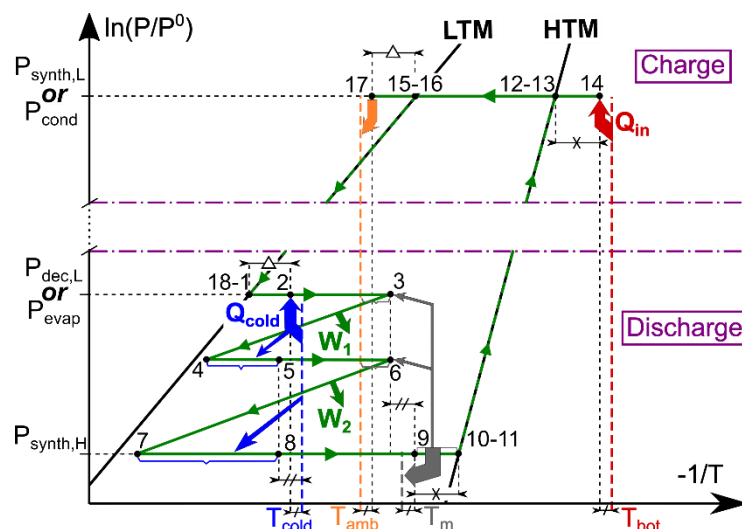


Fig. A1 – Simultaneous power and cold production mode with two expansion stages in the discharging step: thermodynamic path in a Clausius-Clapeyron diagram (see Fig. 3 for captions).

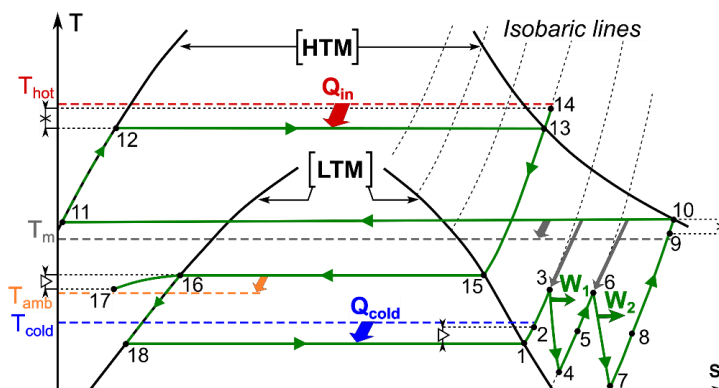


Fig. A2 – Simultaneous power and cold production mode with two expansion stages in the discharging step: thermodynamic path in the T-s diagram of ammonia (see Fig. 3 for captions).

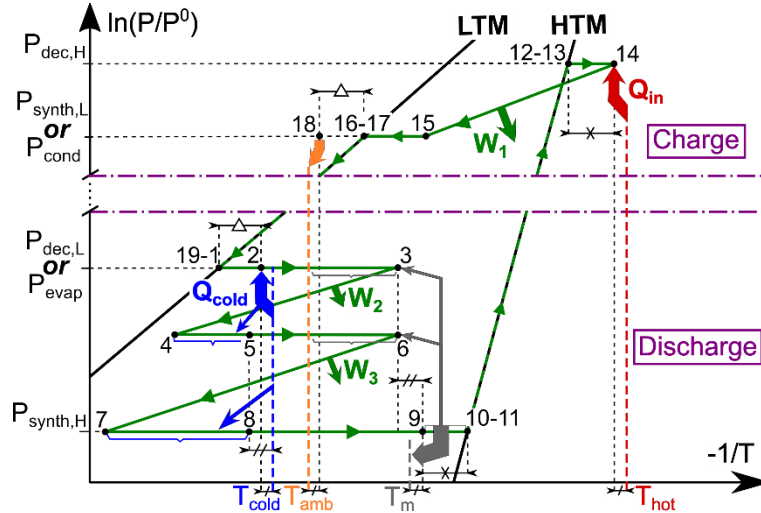


Fig. A3 – Combined power and cold production mode with two expansion stages in the discharging step: thermodynamic path in a Clausius-Clapeyron diagram (see Fig. 3 for captions).

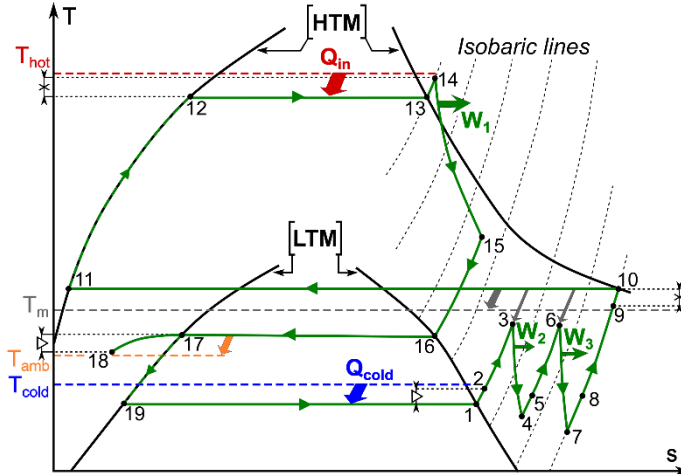


Fig. A4 – Combined power and cold production mode with two expansion stages in the discharging step: thermodynamic path in the T-s diagram of ammonia (see Fig. 3 for captions).

- **Simultaneous** power and cold production with two expansion stages (see Fig. A1 and Fig. A2):

$$W = m_{NH3,cycled} \cdot (h_3 - h_4) + m_{NH3,cycled} \cdot (h_6 - h_7) \quad (A1)$$

$$Q_{in} = n_{NH3,cycled} \cdot \Delta_r H(T_{12}, P_{12}) + [V_{met,H} \cdot \rho_{met} \cdot c_{met} + n_{HTM} \cdot \bar{C}_{HTM}] \cdot (T_{14} - T_9) \quad (A2)$$

$$Q_{cold} = n_{NH3,cycled} \cdot \Delta_r H(T_1, P_1) + m_{NH3,cycled} \cdot (h_5 - h_4) + m_{NH3,cycled} \cdot (h_8 - h_7) - [V_{met,L} \cdot \rho_{met} \cdot c_{met} + n_{LTM} \cdot \bar{C}_{LTM}] \cdot (T_{17} - T_2) \quad (A3a.)$$

$$\text{or} \quad Q_{cold} = n_{NH3,cycled} \cdot L_{vap}(T_1) + m_{NH3,cycled} \cdot (h_5 - h_4) + m_{NH3,cycled} \cdot (h_8 - h_7) - m_{NH3,cycled} \cdot (h_{16} - h_{18}) \quad (A3b.)$$

- **Combined** power and cold production with two expansion stages (see Fig. A3 and Fig. A4):

$$W = m_{NH3,cycled} \cdot (h_3 - h_4) + m_{NH3,cycled} \cdot (h_6 - h_7) + m_{NH3,cycled} \cdot (h_{14} - h_{15}) \quad (A4)$$

$$Q_{in} = n_{NH3,cycled} \cdot \Delta_r H(T_{12}, P_{12}) + [V_{met,H} \cdot \rho_{met} \cdot c_{met} + n_{HTM} \cdot \bar{C}_{HTM}] \cdot (T_{14} - T_9) \quad (A5)$$

$$Q_{cold} = n_{NH3,cycled} \cdot \Delta_r H(T_1, P_1) + m_{NH3,cycled} \cdot (h_5 - h_4) + m_{NH3,cycled} \cdot (h_8 - h_7) - [V_{met,L} \cdot \rho_{met} \cdot c_{met} + n_{LTM} \cdot \bar{C}_{LTM}] \cdot (T_{18} - T_2) \quad (A6a.)$$

$$\text{or} \quad Q_{cold} = n_{NH3,cycled} \cdot L_{vap}(T_1) + m_{NH3,cycled} \cdot (h_5 - h_4) + m_{NH3,cycled} \cdot (h_8 - h_7) - m_{NH3,cycled} \cdot (h_{17} - h_{19}) \quad (A6b.)$$

Appendix B. Additional results

On Fig. B1 to B3, energy and exergy efficiencies using both ‘perfect’ (white symbols) and ‘real’ (solid symbols) sets of assumptions (see Table 1) are plotted for each of the three modes.

Finally, similar to §7.2., the main results are summarized in Fig. B4 to B7. Instead of the regeneration temperature T_{hot} , the x-axis contains all selected salts for the three modes. These plots chart both one-expansion (white symbols) and two-expansions (solid symbols) configurations. Note that regeneration temperatures T_{hot} are plotted on Fig. B4.

Note that the configurations using only one expansion stage have slightly higher energy efficiencies but slightly lower exergy efficiencies than the configurations involving two expansion stages. These small differences are explained by the fact that the cold effect provided at the outlet of the expander(s) (transformation 4-5 on Fig. 5 and Fig. 7, transformations 4-5 and 7-8 on Fig. A1 and Fig. A3) is greater with only one expansion than in two-expansions configurations. On the other hand, two-expansion configurations deliver a greater power output than one-expansion configurations, and hence have higher exergy efficiencies.

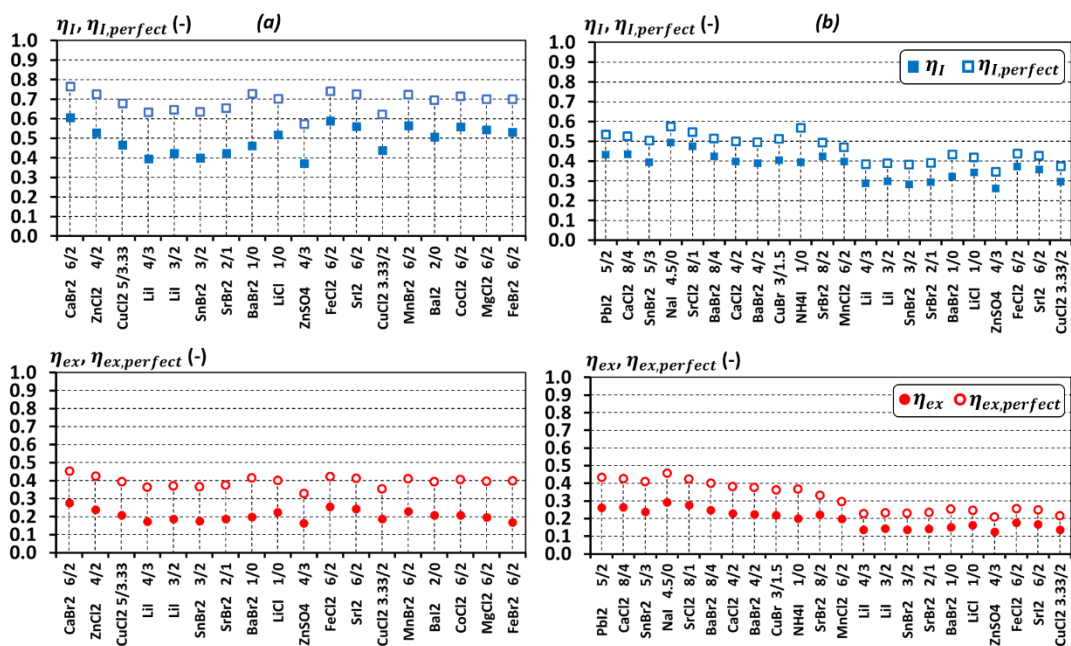


Fig. B1 – Separated power and cold mode: energy and exergy efficiencies of the cycle for selected salts (both ‘perfect’ and ‘real’ cases are plotted)

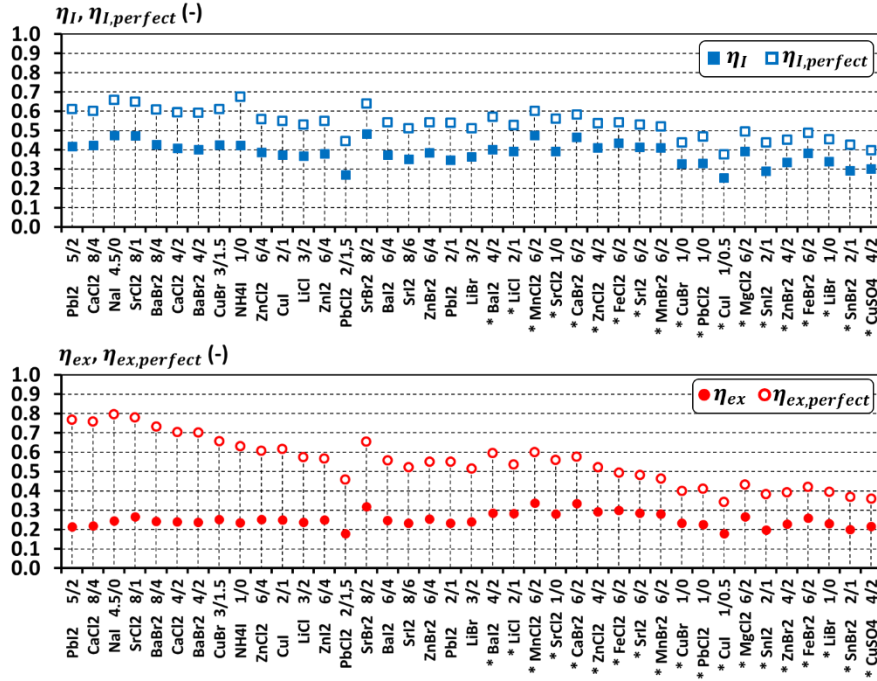


Fig. B2 – Simultaneous power and cold mode: energy and exergy efficiencies of the cycle for selected salts (both 'perfect' and 'real' cases are plotted)

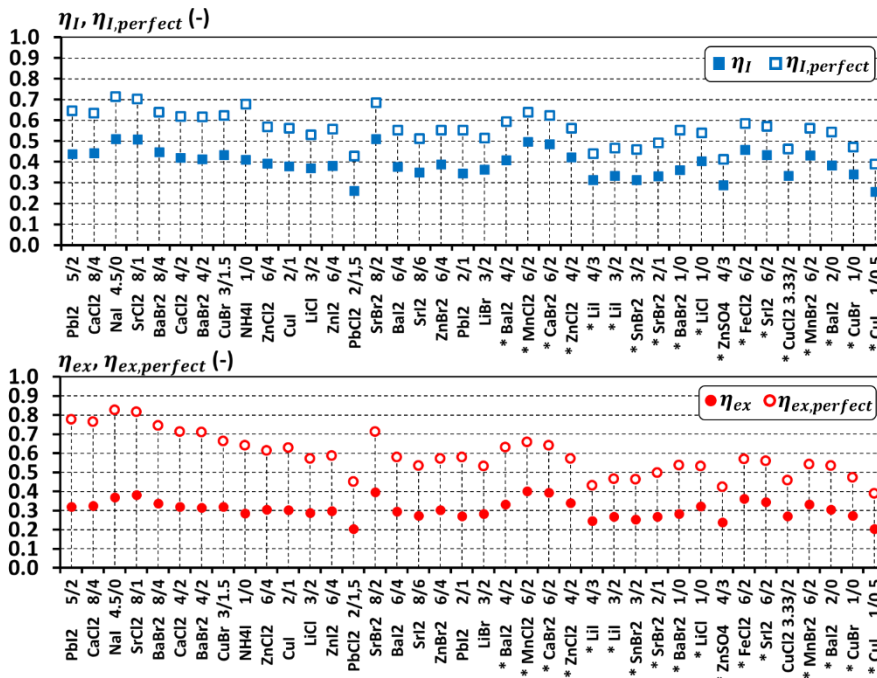


Fig. B3 – Combined power and cold mode: energy and exergy efficiencies of the cycle for selected salts (both 'perfect' and 'real' cases are plotted)

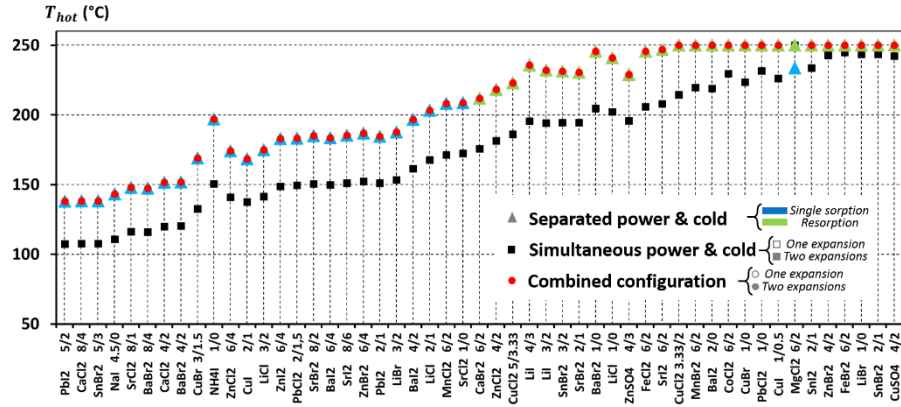


Fig. B4 – Regeneration temperatures: summary of all selected salts in the 3 cogeneration modes

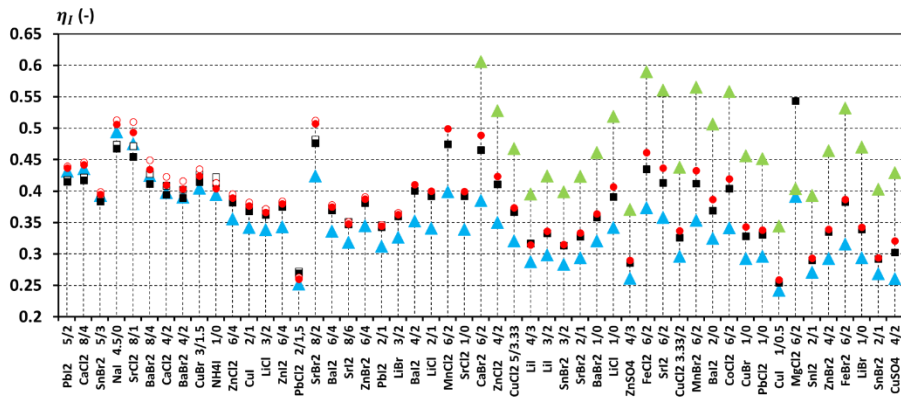


Fig. B5 – Energy efficiencies: summary of all selected salts in the 3 cogeneration modes

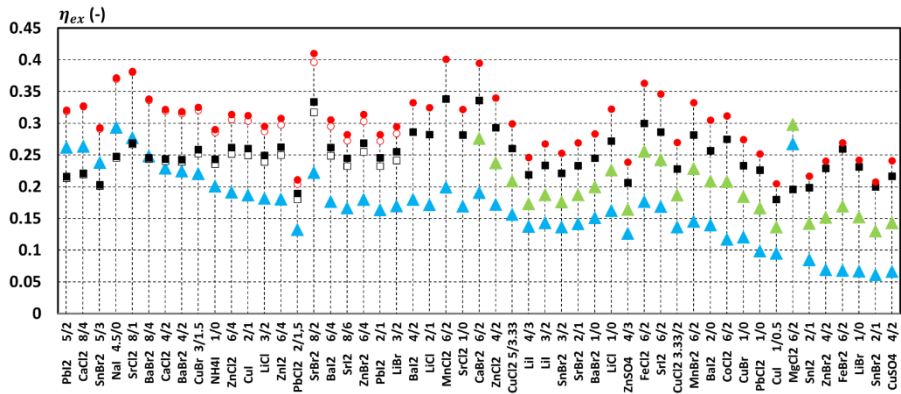


Fig. B6 – Exergy efficiencies: summary of all selected salts in the 3 cogeneration modes

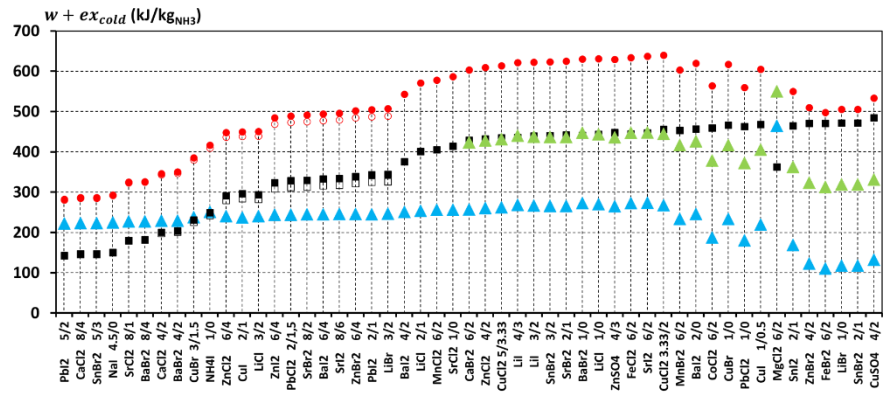


Fig. B7 – Specific exergy outputs: summary of all selected salts in the 3 cogeneration modes